

# A NEW MULTI-DIMENSIONAL GENERAL RELATIVISTIC NEUTRINO HYDRODYNAMICS CODE FOR CORE-COLLAPSE SUPERNOVAE IV. THE NEUTRINO SIGNAL

BERNHARD MÜLLER<sup>1,2</sup>, HANS-THOMAS JANKA<sup>2</sup>

<sup>1</sup>Monash Center for Astrophysics, School of Mathematical Sciences, Building 28, Monash University, Victoria 3800, Australia;  
bernhard.mueller@monash.edu

<sup>2</sup>Max-Planck-Institut für Astrophysik, Karl-Schwarzschild-Str. 1, D-85748 Garching, Germany; bjmuellr@mpa-garching.mpg.de, thj@mpa-garching.mpg.de  
Draft version October 1, 2018

## ABSTRACT

Considering six general relativistic, two-dimensional (2D) supernova (SN) explosion models of progenitor stars between  $8.1$  and  $27 M_{\odot}$ , we systematically analyze the properties of the neutrino emission from core collapse and bounce to the post-explosion phase. The models were computed with the VERTEX-CoCoNuT code, using three-flavor, energy-dependent neutrino transport in the ray-by-ray-plus approximation. Our results confirm the close similarity of the mean energies,  $\langle E \rangle$ , of  $\bar{\nu}_e$  and heavy-lepton neutrinos and even their crossing during the accretion phase for stars with  $M \gtrsim 10 M_{\odot}$  as observed in previous 1D and 2D simulations with state-of-the-art neutrino transport. We establish a roughly linear scaling of  $\langle E_{\bar{\nu}_e} \rangle$  with the proto-neutron star (PNS) mass, which holds in time as well as for different progenitors. Convection inside the PNS affects the neutrino emission on the 10–20% level, and accretion continuing beyond the onset of the explosion prevents the abrupt drop of the neutrino luminosities seen in artificially exploded 1D models. We demonstrate that a wavelet-based time-frequency analysis of SN neutrino signals in IceCube will offer sensitive diagnostics for the SN core dynamics up to at least  $\sim 10$  kpc distance. Strong, narrow-band signal modulations indicate quasi-periodic shock sloshing motions due to the standing accretion shock instability (SASI), and the frequency evolution of such “SASI neutrino chirps” reveals shock expansion or contraction. The onset of the explosion is accompanied by a shift of the modulation frequency below 40–50 Hz, and post-explosion, episodic accretion downflows will be signaled by activity intervals stretching over an extended frequency range in the wavelet spectrogram.

*Subject headings:* supernovae: general—neutrinos—radiative transfer—hydrodynamics—relativity

## 1. INTRODUCTION

Neutrinos play a fundamental role in core-collapse supernovae: Not only do they carry away most (several  $10^{53}$  erg) of the gravitational binding energy liberated during the collapse of the inner shells of the progenitor to a proto-neutron star, they are also the driving agent for the supernova explosion in the most popular scenario for shock revival, the “delayed neutrino-driven mechanism” of Bethe & Wilson (1985); see Janka (2012); Janka et al. (2012); Burrows (2013); Kotake et al. (2012b) for current reviews. Once the explosion has been successfully initiated and post-shock accretion has ceased, the continuing neutrino emission from the proto-neutron star drives a baryonic wind that has long been considered as a site of interesting nucleosynthesis (see, e.g., Arcones & Thielemann 2013).

Moreover, the observation of supernova neutrinos from a future Galactic event could provide tremendous insights into the dynamics deep inside the stellar core and serve to constrain unknown particle physics. The detection of some two dozen neutrinos from Supernova SN 1987A (Hirata et al. 1987; Bionta et al. 1987; Alekseev et al. 1987) already confirmed the basic picture of neutrino emission in core-collapse supernovae, suggesting the emission of  $\sim 3 \times 10^{53}$  erg with a time-averaged neutrino temperature of  $\sim 4$  MeV from a neutrinosphere of the order of a few 10 km with a total signal duration of a few seconds (see, e.g., Arnett et al. 1989; Burrows 1990; Koshiba 1992 for an overview). The signal from SN 1987A also provided constraints on the mass, electric charge, magnetic moment and lifetime of neutrinos as well as indirect constraints on the mass of a hypothetical axion (see Burrows 1990; Keil et al. 1997 and references

therein). Due to much higher event rates, present and next-generation detectors will allow for the reconstruction of the time-dependent neutrino signal in much greater detail (see, e.g., Abe et al. 2011; Wurm et al. 2012 and, for a general overview, Scholberg 2012), which could allow far-reaching conclusions both on the dynamics in the supernova core and open questions in neutrino physics such as the mass hierarchy (Dighe & Smirnov 2000; Serpico et al. 2012).

Quantitatively accurate predictions for the neutrino emission from supernova simulations are an indispensable prerequisite for properly interpreting the neutrino signal from a prospective Galactic event. Nowadays, sophisticated methods for the solution of the neutrino transport problem are available for this purpose. The most advanced schemes for neutrino transport in *spherically symmetric* (1D) neutrino hydrodynamics simulations rely either on the direct solution of the energy-dependent general relativistic (Yamada 1997; Liebendörfer et al. 2004) or Newtonian (Mezzacappa & Bruenn 1993) Boltzmann equation, or on a variable Eddington factor method with Boltzmann closure (Newtonian: Burrows et al. 2000, pseudo-relativistic: Rampp & Janka 2002, general relativistic: Müller et al. 2010; Roberts 2012). These methods have been used to address different phases of the neutrino emission from core-collapse supernovae. Several studies focused specifically on the neutronization burst (Kachelrieß et al. 2005; Langanke et al. 2008) and the rise of the electron antineutrino and the heavy flavor neutrino luminosity (Serpico et al. 2012) around shock breakout (with an emphasis on the detectable signal). The dependence of the neutrino emission during the pre-explosion (accretion) phase on the progenitor properties and the equation of state (EoS) of nuclear matter has been

the subject of a larger number of papers (Thompson et al. 2003; Liebendörfer et al. 2003; Sumiyoshi et al. 2005; Buras et al. 2006a; Fischer et al. 2009; O’Connor & Ott 2013; Nakazato et al. 2013). Sumiyoshi et al. (2008) and Fischer et al. (2009) also cover the case of black hole formation in failed supernovae. Lentz et al. (2012b,a) recently studied the impact of variations in the microphysics and approximations in the neutrino transport sector and emphasized the importance of a rigorous treatment of general relativity, observer corrections, and energy-exchanges in scattering reactions on electrons and nucleons for accurate predictions of neutrino luminosities and mean energies.

1D simulations using multi-group Boltzmann or variable Eddington factor transport have likewise been used to predict the signal from the Kelvin-Helmholtz cooling phase after the successful initiation of an explosion (Hüdepohl et al. 2009; Fischer et al. 2010, 2012; Roberts 2012; Roberts et al. 2012b; Martínez-Pinedo et al. 2012). However, with the exception of electron-capture supernovae (Hüdepohl et al. 2009; Fischer et al. 2010), predictions for the neutrino signal from the post-explosion phase are currently based on *artificial* explosion models in which shock revival is achieved by manually boosting neutrino heating in the gain layer, or even start from initial models of the proto-neutron star constructed by hand (Roberts 2012; Roberts et al. 2012b).

According to our current understanding, neutrino-driven core-collapse supernovae are inherently *multi-dimensional* (multi-D). Hydrodynamic instabilities like buoyancy-driven convection in the neutrino-heated gain region (Bethe 1990; Herant et al. 1992, 1994; Burrows et al. 1995; Janka & Müller 1996; Müller & Janka 1997) and the standing accretion shock instability (“SASI”, Blondin et al. 2003; Blondin & Mezzacappa 2006; Foglizzo et al. 2006; Ohnishi et al. 2006; Foglizzo et al. 2007; Scheck et al. 2008; Iwakami et al. 2008, 2009; Fernández & Thompson 2009; Fernández 2010) were found to play a crucial role in the explosion mechanism, and they are no less relevant for the neutrino emission. However, predictions for the neutrino signal from multi-D supernova simulations with a transport treatment on par with the best available 1D models are still scarce. Attempts at a rigorous solution of the 3D Boltzmann equation (Kotake et al. 2012a; Radice et al. 2013; Peres et al. 2014) are yet in their infancy. The best available studies of multi-D effects on the neutrino emission therefore either rely on Newtonian 2D multi-angle transport with considerable compromises in the microphysics and omission of energy-bin coupling (Ott et al. 2008; Brandt et al. 2011) or on multi-group variable Eddington factor transport using the “ray-by-ray-plus approximation” of Buras et al. (2006b); Bruenn et al. (2006) in 2D (Marek et al. 2009; Lund et al. 2010) and 3D (Tamborra et al. 2013). Predictions for the explosion phase are currently available only from parameterized models with gray transport and an excised neutron star core (Müller et al. 2012c; Lund et al. 2012). Despite the different methodologies there is a consensus that the neutrino signal is considerably affected by multi-D instabilities. Asymmetric accretion onto the proto-neutron star gives rise to spatial anisotropies and temporal variations in the neutrino emission. These spatio-temporal variations show a distinct imprint of the different hydrodynamic instabilities in the supernova core, with SASI oscillations leading to fluctuations in the neutrino signal with a rather well-defined frequency around 100 Hz, and convective overturn resulting in more stochastic variations (Tamborra et al. 2013). After the onset of the

explosion, the neutrino emission is typically characterized by large-scale spatial anisotropies as the accretion flow onto the proto-neutron star (which usually subsists for several hundreds of milliseconds after shock revival) becomes highly asymmetric.

In this paper, we reexamine the neutrino emission in core-collapse supernovae on the basis of state-of-the-art axisymmetric (2D) general relativistic simulations with energy-dependent three-flavor neutrino transport. We consider a wide range of progenitors from the lowest-mass iron cores, where multi-D effects play a minor role for the neutrino emission, through more massive models with vigorous convection and SASI. Different from previous studies of neutrino emission in multi-D simulations of the post-bounce phase (Ott et al. 2008; Marek et al. 2009; Lund et al. 2010; Brandt et al. 2011; Tamborra et al. 2013), we explore both the pre-explosion and the explosion phase. We analyze both the overall secular evolution of the neutrino emission as well as spatio-temporal variations on shorter time-scales. In order to connect with future neutrino observations, we show how the quantitative analysis of the signal from a prospective Galactic event in a detector like IceCube (Abbasi et al. 2011; Salathe et al. 2012) could provide detailed time-dependent information about the dynamics in the supernova core.

Our paper is structured as follows: In Section 2, we outline the numerical methods and the input physics of our simulations, including the progenitor models. In Section 3, we review the secular evolution of the spherically averaged neutrino luminosities and mean energies. In Section 4, we discuss the spatio-temporal variations in the neutrino emission on the basis of simulated IceCube signals. By means of a time-frequency analysis using wavelet transforms, we show that the IceCube signal can reveal the detailed time-dependence of the SASI sloshing frequency, the rough evolution of the shock radius, the onset of the explosion, and early fallback onto the proto-neutron star through newly-formed accretion funnels. In Section 5, we summarize our findings, examine their robustness, and discuss further implications for the observation of a future Galactic supernova in gravitational waves and neutrinos.

## 2. NUMERICAL METHODS AND MODEL SETUP

We study the neutrino emission in six axisymmetric (2D) core-collapse supernova simulations computed with the general relativistic neutrino hydrodynamics code VERTEX-CoCoNuT (Müller et al. 2010, paper I in this series). For full details, the reader should consult paper I, since we confine ourselves to a very brief outline of the code methodology in this section.

### 2.1. Hydrodynamics and Gravity

The hydrodynamics module CoCoNuT is a general relativistic finite-volume solver using higher-order PPM reconstruction (Colella & Woodward 1984) and the approximate HLLC Riemann solver (Mignone & Bodo 2005) modified to avoid odd-even decoupling and the carbuncle phenomenon at strong shocks (Quirk 1994). The metric equations are solved in the extended conformal flatness approximation (xCFC) of Cordero-Carrión et al. (2009).

### 2.2. Neutrino Transport

The neutrino transport module VERTEX integrates the energy-dependent zeroth and first moment equations for neu-

**Table 1**  
Neutrino physics input

process	reference
$\nu A \rightleftharpoons \nu A$	Horowitz (1997) (ion-ion correlations)
	Langanke et al. (2008) (inelastic contribution)
$\nu e^\pm \rightleftharpoons \nu e^\pm$	Mezzacappa & Bruenn (1993)
$\nu N \rightleftharpoons \nu N$	Burrows & Sawyer (1998) <sup>a</sup>
$\nu_e n \rightleftharpoons e^- p$	Burrows & Sawyer (1998) <sup>a</sup>
$\bar{\nu}_e p \rightleftharpoons e^+ n$	Burrows & Sawyer (1998) <sup>a</sup>
$\nu_e A' \rightleftharpoons e^- A$	Langanke et al. (2003)
$\nu \bar{\nu} \rightleftharpoons e^- e^+$	Bruenn (1985); Pons et al. (1998)
$\nu \bar{\nu} NN \rightleftharpoons NN$	Hannestad & Raffelt (1998)
$\nu_{\mu,\tau} \bar{\nu}_{\mu,\tau} \rightleftharpoons \nu_e \bar{\nu}_e$	Buras et al. (2003)
$\begin{pmatrix} (-) & (-) & (-) & (-) \\ \nu_{\mu,\tau} & \nu_e & \bar{\nu}_{\mu,\tau} & \bar{\nu}_e \end{pmatrix}$	Buras et al. (2003)

<sup>a</sup> Note that these reaction rates account for nucleon thermal motions, phase-space blocking, energy transfer to the nucleon associated with recoil (“non-conservative” or “non-isoenergetic” scattering), and nucleon correlations at high densities. Moreover, we include the quenching of the axial-vector coupling at high densities (Carter & Prakash 2002), correction to the effective nucleon mass (Reddy et al. 1999), and weak magnetism effects (Horowitz 2002). However, we ignore nucleon potential effects (Martínez-Pinedo et al. 2012; Roberts et al. 2012a), which are of minor importance during the accretion phase (Martínez-Pinedo et al. 2012).

**Table 2**  
Model setup

progenitor	metallicity $Z/Z_\odot$	angular resolution	explosion obtained	time of explosion <sup>a</sup>	EoS	progenitor reference	simulation reference
u8.1	$10^{-4}$	$1.4^\circ$	yes	175 ms	LS180	A. Heger (private communication)	Müller et al. (2012a)
z9.6	0	$1.4^\circ$	yes	125 ms	LS220	A. Heger (private communication)	Müller et al. (2013)
s11.2	1	$2.8^\circ$	yes	213 ms	LS180	Woosley et al. (2002)	Müller et al. (2012b)
s15s7b2	1	$2.8^\circ$	yes	569 ms	LS180	Woosley & Weaver (1995)	Müller et al. (2012b)
s25	1	$1.4^\circ$	no	—	LS220	Woosley et al. (2002)	Müller et al. (2013)
s27	1	$1.4^\circ$	yes	209 ms	LS220	Woosley et al. (2002)	Müller et al. (2012a)

<sup>a</sup> Defined as the point in time when the average shock radius  $\langle r_{\text{sh}} \rangle$  reaches 400 km.

trino and antineutrinos of all flavors using a variable Eddington factor technique (Rampp & Janka 2002). We resort to the “ray-by-ray-plus” approximation (Buras et al. 2006b) to make the multi-D transport problem tractable. In the ray-by-ray-plus approach, the radiation field is assumed to be axially symmetric around the radial unit vector, which effectively decouple the neutrino transport problem along different rays through the origin. However, the lateral advection of neutrinos with the fluid is included in an operator-split fashion, as is the lateral neutrino pressure gradient in the optically thick regime. It should be pointed out that the ray-by-ray-plus approximation does *not* imply that neutrinos propagate only in the radial direction, it merely implies that the energy flux vector is radial and that lateral gradients (except for advection terms) in the moment equations are neglected. The ray-by-ray-plus approach allows us to predict angular variations in the neutrino radiation field at least in rough qualitative agreement with full multi-angle transport (Ott et al. 2008; Brandt et al. 2011). Full multi-angle transport smears out angular variations in the radiation field at larger radii, especially outside the neutrinosphere. In order to obtain better quantitative estimates for the angular variations at large distances from the proto-neutron star, we therefore reprocess our simulation data to obtain observable neutrino fluxes using the method introduced by Müller et al. (2012c) as described in Section 4.1.

The moment equations solved along each ray fully include relativistic effects (Müller et al. 2010) and energy redistribu-

tion in “inelastic” or “non-conservative” scattering reactions. An up-to-date set of neutrino interactions rates, briefly summarized in Table 1, has been used for the simulations presented in this paper. All models were computed with the “full set” of Müller et al. (2012b).

### 2.3. Progenitor Models and Core-Collapse Simulations

We have simulated the collapse and post-bounce evolution of non-rotating progenitors with  $8.1M_\odot$ ,  $9.6M_\odot$ ,  $11.2M_\odot$ ,  $15M_\odot$ ,  $25M_\odot$ , and  $27M_\odot$ . The  $8.1M_\odot$  (u8.1) and  $9.6M_\odot$  (z9.6) stars (A. Heger, private communication) are progenitors close to the lower mass limit for iron core formation at metallicities of  $Z = 10^{-4}$  and  $Z = 0$ , respectively. These stars explode very quickly with little help from convection and the SASI. Three progenitors (s11.2, s25, s27) have been taken from Woosley et al. (2002) and serve as examples for a relatively fast but rather weak convectively-dominated explosion (s11.2), a fast SASI-dominated explosion (s27), and a SASI-dominated model (s25), which fails to explode until more than 600 ms after bounce and shows little promise for a successful explosion at later times. Model s15s7b2 from Woosley & Weaver (1995) illustrates the case of a late explosion. The dynamics of these models has already been discussed in much detail elsewhere (Müller et al. 2012b,a, 2013; Janka et al. 2012).

The core-collapse simulations have been conducted using the equation of state of Lattimer & Swesty (1991) with a bulk

incompressibility modulus of  $K = 220$  MeV (LS220) for models z9.6, s25, and s27, and with  $K = 180$  MeV (LS180) for u8.1, s11.2, and s15s7b2. For the neutron star masses encountered in these two cases, LS220 and LS180 yield very similar results because of very similar proto-neutron star radii as discussed in Müller et al. (2013), and the incompatibility of LS180 with the observed maximum neutron star mass of  $\approx 2M_\odot$  (Demorest et al. 2010) is therefore of no immediate concern. We expect only a weak dependence of the model dynamics and the neutrino signal on the choice of bulk incompressibility ( $K = 220$  MeV vs.  $K = 180$  MeV) for these two EoS's.

Models s11.2 and s15s7sb2 have been simulated with a reduced angular resolution of  $2.8^\circ$  (64 zones) instead of  $1.4^\circ$  (128 zones). The setup of the six simulations is summarized in Table 2, including references for more details on the model evolution and dynamics.

### 3. OVERVIEW OF NEUTRINO LUMINOSITIES AND MEAN ENERGIES

The emission of neutrinos from the supernova core is regulated by physical processes with very different time-scales. The diffusion of neutrinos from the interior of the hot proto-neutron star to the neutrinosphere provides a steady, slowly-varying source for neutrinos of all flavors (and is the dominant source for heavy flavor neutrinos). This diffusive component originates from the spherically stratified and roughly isentropic accretion mantle of the proto-neutron star with densities  $\gtrsim 10^{13}$  g cm $^{-3}$ , and is almost isotropic in the absence of rotation. Electron neutrinos and antineutrinos are also copiously emitted from the “cooling region” outside the neutrinosphere at optical depth  $\lesssim 1$ , where fresh material is continually resupplied as long as accretion onto the proto-neutron star continues. The total accretion luminosity  $L_{\text{acc}}$  is roughly given by the mass accretion rate  $\dot{M}$  and the gravitational potential at the neutron star surface (Burrows 1988; Fischer et al. 2009),

$$L_{\text{acc}} \approx \frac{GM\dot{M}}{r_{\text{PNS}}}, \quad (1)$$

where  $M$  and  $r_{\text{PNS}}$  are the proto-neutron star mass and radius.  $L_{\text{acc}}$  can vary on much shorter time-scales (milliseconds to tens of milliseconds) than the diffusive luminosity provided that  $\dot{M}$  changes rapidly. If the accretion flow is asymmetric due to convection or the SASI, the emission from the cooling region can also become strongly anisotropic. Generally, the emission anisotropies will be short-lived with a typical time-scale identical to that of the underlying hydrodynamic instability, i.e. a few tens of milliseconds or less during the accretion phase.

It is expedient to separate the discussion of the neutrino emission on different temporal and spatial scales. The secular variation of the angle-integrated “monopole” component of the neutrino radiation field can be analyzed largely without taking the action of convection and the SASI into account. To this end, we compute the angle-integrated neutrino energy flux (“total luminosity”  $L_{\text{tot},i}$ ) of neutrino flavor  $i$ ,

$$L_{\text{tot},i} = \int \alpha^2 \phi^4 F_{\text{eul}}(r = 400\text{km}) r^2 d\Omega, \quad (2)$$

and the angle-averaged mean energy  $\langle E_i \rangle$ ,

$$\langle E_i \rangle = \frac{\int \alpha^2 \phi^4 F_{\text{eul}}(r = 400\text{km}) d\Omega}{\int \alpha \phi^4 \mathcal{F}_{\text{eul}}(r = 400\text{km}) d\Omega}, \quad (3)$$

for our six 2D models. Here  $F_{\text{eul}}$  and  $\mathcal{F}_{\text{eul}}$  are the lab-frame neutrino energy flux and number flux, respectively, and  $\alpha$  and  $\phi$  are the lapse function and conformal factor in the CFC metric. The neutrino luminosities and mean energies are extracted at a radius of 400 km, where they have essentially reached their asymptotic values. The total neutrino fluxes  $L_{\text{tot},i}$  and the corresponding mean energies  $\langle E_i \rangle$  are shown as functions of time in Figure 1. We also show the temporal evolution of important parameters of the proto-neutron star and the accretion flow, which determine the neutrino luminosities and mean energies in Figures 2 and 3. Figure 2 presents the time evolution of the baryonic mass of the proto-neutron star (defined as the total amount of material at densities exceeding  $10^{11}$  g cm $^{-3}$ ) and the (baryonic) mass accretion rate  $\dot{M}$  (measured at a radius of 400 km). The contraction of the proto-neutron star radius  $r_{\text{PNS}}$  is shown in Figure 3.

#### 3.1. Neutrino Burst and Early Accretion Phase

The first prominent feature in Figure 1 is the well-known electron neutrino or neutronization burst that occurs when the post-shock matter becomes optically thin shortly after bounce as the newly-formed shock propagates outwards (“shock breakout”). As the post-shock region is far away from neutrino-less beta-equilibrium, electron captures on protons quickly produce a large number of electron neutrinos at this stage.

The neutronization burst signal in  $\nu_e$  is rather homogeneous across the different progenitors (in agreement with Mayle et al. 1987; Liebendörfer et al. 2003; Kachelrieß et al. 2005) with a maximum luminosity of  $(3.3 \dots 4.4) \times 10^{53}$  erg s $^{-1}$ , an interval bracketed by models s15s7b2 and s25 on the lower and upper end. There is even less spread in the peak mean energy of electron neutrinos  $\langle E_{\nu_e} \rangle$  reached during the burst, which ranges from 12.9 MeV (s15s7b2) to 14.2 MeV (z9.6).

As the  $\nu_e$  burst subsides, the flux of  $\bar{\nu}_e$  and  $\nu_{\mu/\tau}$  starts to rise. While the emission of  $\bar{\nu}_e$  is initially suppressed due to a relatively high electron fraction around the neutrinosphere and in the cooling region above it (which implies strong electron degeneracy), leading to a delayed rise of  $\bar{\nu}_e$ 's compared to the  $\nu_{\mu/\tau}$ 's, the  $\bar{\nu}_e$ 's eventually reach a flux similar to the  $\nu_e$ 's. The excess of electron (anti)neutrino emission compared to the heavy flavor neutrinos is due the contribution from accretion and is hence progenitor-dependent; for the low-mass progenitors u8.1 and z9.6, it is never very pronounced, whereas the electron neutrino and antineutrino luminosities can be larger almost by a factor of two for more massive progenitors.

Interestingly, the different progenitors show a different luminosity hierarchy of electron neutrinos and antineutrinos during the early accretion phase with an early crossing around  $\sim 60$  ms after bounce in the case of models s11.2 and s15s7b2 where the  $\bar{\nu}_e$  luminosity slightly exceeds the  $\nu_e$  luminosity (a phenomenon observed even more strongly in the  $12M_\odot$  model simulated by Bruenn et al. 2013). This is a subtle effect that cannot be connected to the surface properties of the proto-neutron star. During this early phase, neutrinos are emitted from a very extended region, and for electron neutrinos, emission still dominates over absorption all the way to the shock due to the deleptonization of the infalling matter. By contrast, a considerable fraction of the electron antineutrinos is absorbed in the region where net heating develops later on. The different balance between emission and absorption in the post-shock region results in a considerable re-adjustment for the electron flavor luminosities from the proto-neutron

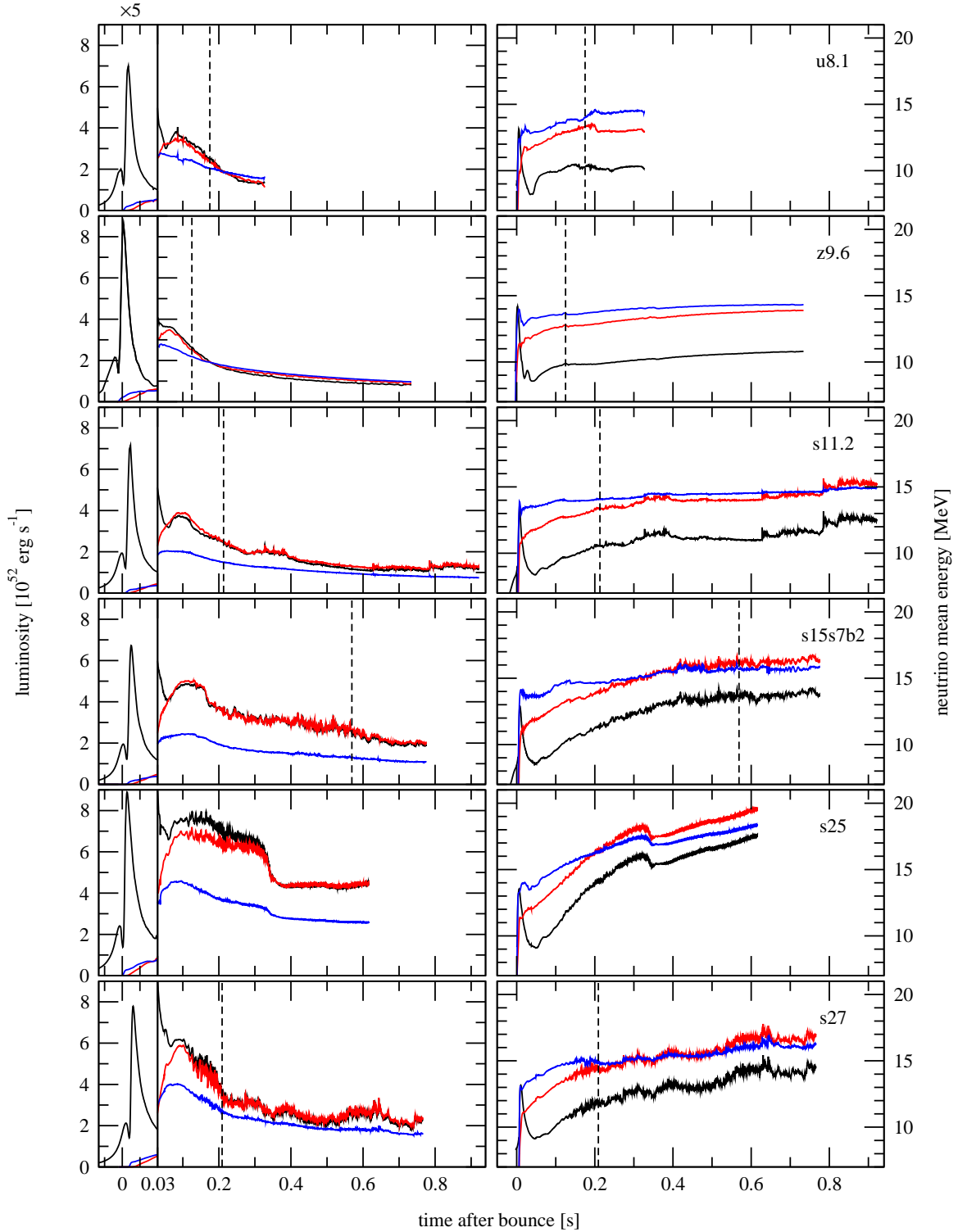


**Figure 1.** Total energy loss rates (“luminosities”),  $L_{\text{tot}}$  (left column), and mean energies,  $\langle E \rangle$  (right column), of the emitted neutrinos for models u8.1, z9.6, s11.2, s15s7b2, s25, and s27 (from top to bottom). Black, red, and blue curves are used for electron neutrinos, electron antineutrinos, and  $\mu/\tau$  neutrinos, respectively. Note that a different scale is used prior to a post-bounce time of 30 ms in order to fit the neutrino shock-breakout burst into the same plot as the signal from the accretion phase: During the burst phase, the luminosities have been scaled down by a factor of 5, i.e. the reader should understand that the actual luminosity is higher by that factor. A dashed vertical line marks the onset of the explosion (defined as the time when the average shock radius reaches 400 km) in exploding models.

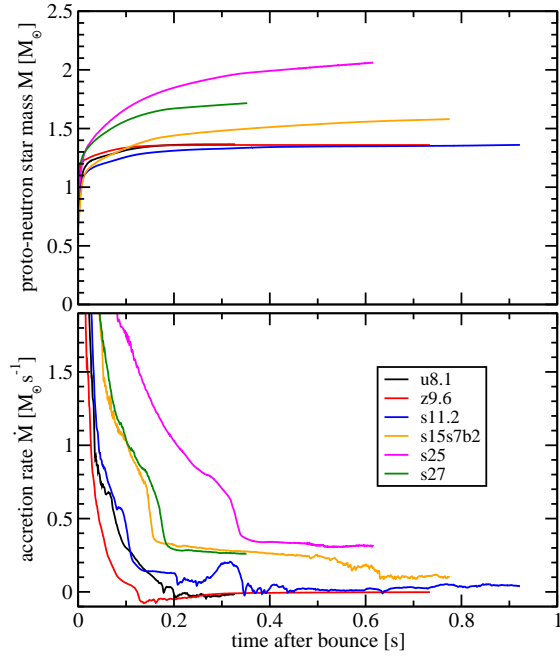


**Figure 2.** Baryonic proto-neutron star mass  $M$  (top) and mass accretion rate  $\dot{M}$  (bottom, measured at a radius of 500 km) for models u8.1, z9.6, s11.2, s15s7b2, s25, and s27. The bumps in  $M$  around 300 ms in the case of the  $11.2 M_\odot$  model are a consequence of a temporary expansion of the shock beyond 500 km.

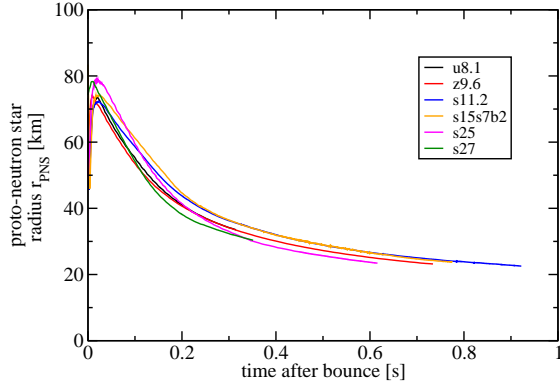


**Figure 3.** Evolution of the circumferential radius  $r_{\text{PNS}}$  of the proto-neutron star (defined by a fiducial density of  $10^{11} \text{ g cm}^{-3}$ ) for models u8.1, z9.6, s11.2, s15s7b2, s25, and s27.

star surface and deeper layers of the cooling region, as we show in Figure 4 for model s27, which does not show the early crossing of  $\nu_e$  and  $\bar{\nu}_e$  luminosities. Moreover, proto-neutron star convection affects electron neutrino and antineutrino luminosities differently at early stages, generally tilting the balance in favor of electron neutrinos by transporting lepton number from deeper layers into the neutrinosphere region (Buras et al. 2006b). The hierarchy of electron neutrino and antineutrino luminosities during the early phase thus seems almost accidental, and is certainly very sensitive to small variations in the models (such as the extent of the region affected by proto-neutron star convection and the exact temporal decay behavior of the mass accretion rate in the early post-bounce phase).

### 3.2. Later Accretion Phase – Luminosities

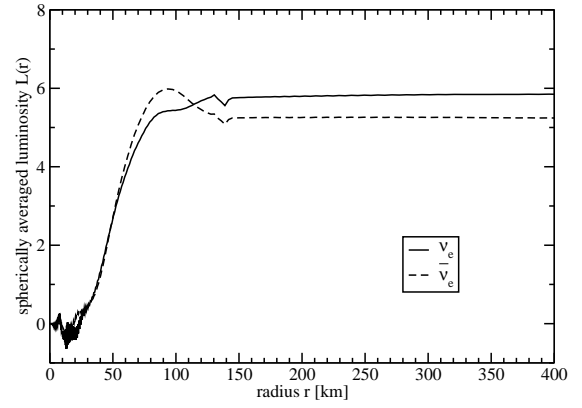


**Figure 4.** Radial profiles of  $L_{\nu_e}$  and  $L_{\bar{\nu}_e}$  during the early accretion phase (70 ms after bounce) for model s27. The hierarchy of the luminosities at infinity  $L_{\nu_e} > L_{\bar{\nu}_e}$  is inverted compared to the luminosities just outside the proto-neutron star ( $r \approx 90$  km), because emission dominates over absorption for electron neutrinos in the post-shock region, while the electron antineutrino luminosity is reduced considerably between 90 km and 140 km due to net absorption. The kink at  $\sim 140$  km coincides with the shock position and is an artifact of the transformation from the comoving frame to the lab frame.

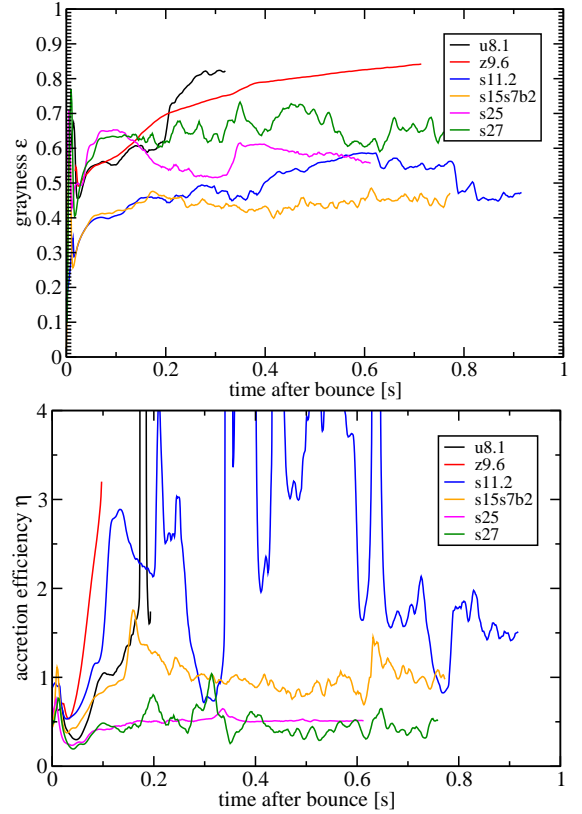


**Figure 5.** Grayness parameter  $\epsilon$  for the emission of  $\mu$  and  $\tau$  neutrinos (top panel) and accretion efficiency  $\eta$  (bottom panel) for all models. Note that the accretion efficiency is computed using the mass accretion rate  $\dot{M}$  at  $r = 500$  km.

During the later accretion phase, the electron neutrino and antineutrino luminosities are largely regulated by the mass accretion rate  $\dot{M}$  (Fischer et al. 2009). For high  $\dot{M}$ , the total electron flavor luminosity is of the order of the accretion luminosity  $L_{\nu_e} + L_{\bar{\nu}_e} \sim G\dot{M}/r_{\text{PNS}}$  ( $M$  and  $r_{\text{PNS}}$  being the mass and radius of the proto-neutron star, respectively), though it may deviate by a few tens of percent.

As the accretion rate drops, the relative contribution of

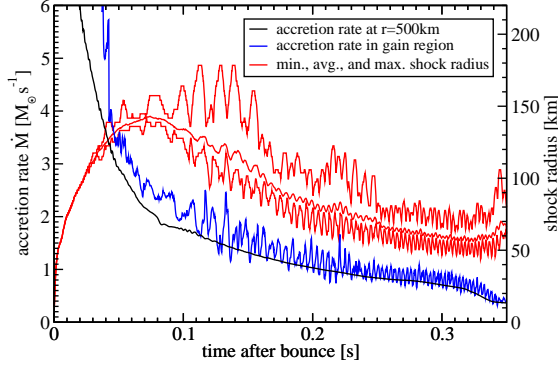


**Figure 6.** Accretion rate  $\dot{M}$  ahead of the shock at  $r = 500$  km (black) and between the gain radius and average shock radius at  $r = (r_{\text{gain}} + r_{\text{sh}})/2$  (blue) for model s25. The minimum, average and maximum shock radii are also shown (red). The (small) periodic expansion and retraction of the average radius is reflected in a relatively strong quasi-periodic modulation of the accretion rate in the gain region. As a result of the fluctuating supply of material into the cooling region, there is a small periodic variation in the total neutrino luminosity (see fifth row in Figure 1). Only the first  $\sim 350$  ms after bounce are shown to make the fluctuations more clearly visible. Compare the fifth row in Figure 1 for the resulting modulation of the electron neutrino and antineutrino luminosities.

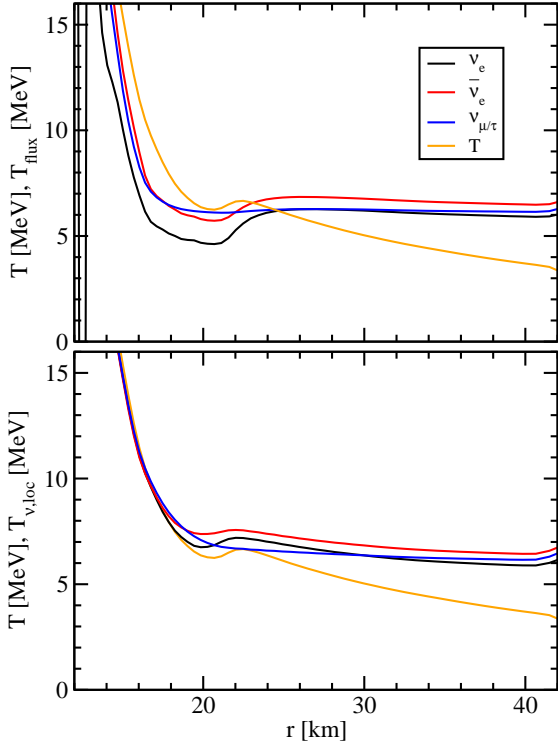


**Figure 7.** Radial profiles of the flux temperature  $T_{\text{flux}}$  (top panel, Equation 6) and the local temperature  $T_{\text{v,loc}}$  (bottom panel, Equation 7) for the different neutrino species compared to the matter temperature  $T$  at a post-bounce time of 591 ms for model s25.  $T_{\text{v,eff}}$  follows the matter temperature closely deep in the optically thick regime, but starts to deviate from  $T$  well before its asymptotic value is reached.  $T_{\text{flux}}$  is generally lower than  $T$  at high optical depths.  $T_{\text{flux}}$  approaches or crosses  $T$  where energy-exchanging reactions freeze out and reaches it asymptotic value close to that point.

the electron neutrino and antineutrino flux from diffusion out of the deeper PNS core becomes more appreciable. Rapid changes in  $\dot{M}$  due to the infall of composition interfaces in the progenitor result in pronounced steps in the luminosity of  $\nu_e$  and  $\bar{\nu}_e$  (see Figure 1). The heavy flavor neutrinos show a steady decline and are not sensitive to sudden variations in  $\dot{M}$ .

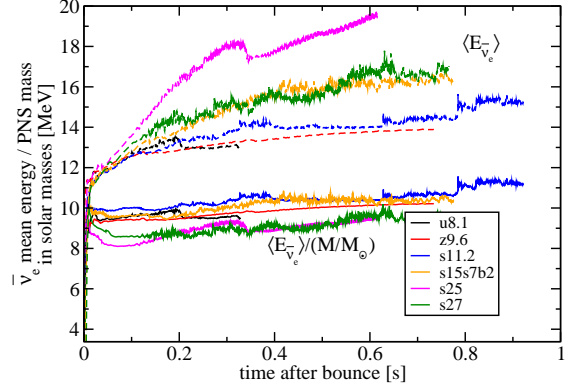


**Figure 8.** Time evolution of the electron antineutrino mean energy  $\langle E_{\bar{\nu}_e} \rangle / (M/M_\odot)$  rescaled by the proto-neutron star mass  $M$  for the different progenitors. The mean energies  $\langle E_{\bar{\nu}_e} \rangle$  themselves are shown as dashed lines along with the rescaled mean energies  $\langle E_{\bar{\nu}_e} \rangle / (M/M_\odot)$  (solid lines). When comparing different progenitors the reader should note that models s11.2 and s15s7b2 have been computed with an angular resolution of  $2.8^\circ$  instead of  $1.4^\circ$  (u8.1, z9.6, s25, s27), and that two different EoS's have been used (u8.1, s11.2, s15s7b2: LS180; z9.6, s25, s27: LS220).

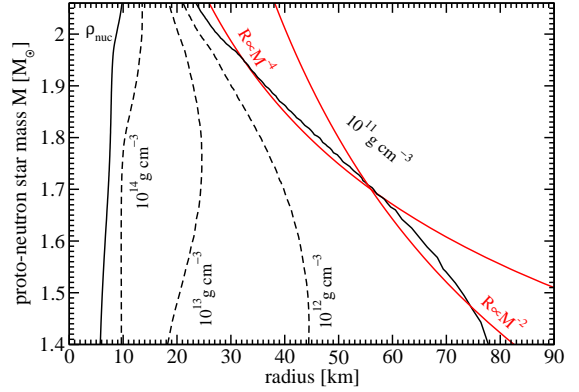


**Figure 9.** Mass-radius relation for different density isosurfaces as observed during the evolution of model s25. The black curves are defined by the baryonic mass  $M$  of the *entire* proto-neutron star (i.e. the mass contained in the density isosurface for  $10^{11} \text{ g cm}^{-3}$ ) and the radius corresponding to different densities (nuclear saturation density  $\rho_{\text{nuc}}$ ,  $10^{14} \text{ g cm}^{-3}$ ,  $10^{13} \text{ g cm}^{-3}$ ,  $10^{12} \text{ g cm}^{-3}$ , and  $10^{11} \text{ g cm}^{-3}$ ). The curves for nuclear saturation density and the density of  $10^{11} \text{ g cm}^{-3}$  (which we use to define the proto-neutron star radius in this paper) are shown as solid lines; curves for other densities are shown as dashed lines. Curves for power laws  $R \propto M^{-4}$  and  $R \propto M^{-2}$  are shown in red for comparison. It should be noted that the high-density core retains a relatively constant radius as the proto-neutron star accretes. The outer layers contract strongly with increasing  $M$ .

Although the neutrino luminosities during the accretion phase are related to the proto-neutron star parameters, quantitative deductions from the luminosities appear difficult. For the heavy flavor neutrinos, one can assume a simple gray body ansatz in terms of the neutron star surface temperature  $T_\nu$  and radius  $r_{\text{PNS}}^2$ ,

$$L_{\nu\mu/\tau} = 4\pi\epsilon\sigma_{\text{fermi}}r_{\text{PNS}}^2T_\nu^4. \quad (4)$$

Here,  $\sigma_{\text{fermi}} = 4.50 \times 10^{35} \text{ erg MeV}^{-4} \text{ s}^{-1} \text{ cm}^{-2}$  is the radiation constant for neutrinos as left- or right-handed fermions of zero degeneracy,  $T_\nu$  is an effective surface temperature approximately given by  $\langle E_{\bar{\nu}_e} \rangle / 3.15$ , and the grayness factor  $\epsilon$  accounts for deviations from black body emission. Figure 5 shows a considerable spread in  $\epsilon$  across the progenitors as well as strong non-monotonic time variations. We obtain values in the range  $\epsilon = 0.4 \dots 0.85$ , which is compatible with the findings of H  dephohl et al. (2009) for an electron-capture



supernova during the first second.

Similarly, the accretion rate  $\dot{M}$  can only be inferred very tentatively from the luminosities. The accretion luminosity  $L_{\text{acc}}$  is already difficult to separate from the diffusive (gray body) contribution to begin with. As long as it is sufficiently high, the excess of the electron (anti)neutrino luminosity over the (anti)neutrino luminosity of a single heavy flavor may be taken as a proxy for  $L_{\text{acc}}$ , which may then be related to the accretion rate  $\dot{M}$  by introducing an efficiency parameter  $\eta$ ,

$$L_{\text{acc}} \approx L_{\nu_e} + L_{\bar{\nu}_e} - 2L_{\nu_{\mu/\tau}} = \eta \frac{GM\dot{M}}{r_{\text{PNS}}}. \quad (5)$$

The bottom panel of Figure 5 shows that for the less massive progenitors (u8.1, z9.6, s11.2) the subtraction of a diffusive component works up to shock revival at best, where  $\eta \approx 1$ . Afterwards,  $\eta$  increases steeply as the accretion rate  $\dot{M}$  plummets. For models with an extended accretion phase continuing beyond the onset of the explosion (s15s7b2, s25, s27), we find  $\eta \approx 0.5 \dots 1$  most of the time even after shock revival.

It is noteworthy that even the (directionally averaged) luminosity shows marked temporal fluctuations in models with strong activity of the SASI and/or convection, such as s15s7b2, s25, and s27. These fluctuations are a consequence of oscillations in the angle-averaged shock radius, resulting in a periodic increase and decrease of the rate of mass accretion  $\dot{M}_{\text{cool}}$  into the cooling region as shown in Figure 6. However, in the observable signal for a fixed viewing angle these variations in the angle-integrated luminosity are dwarfed by spatio-temporal variations in the neutrino emission, which are discussed at length in Section 4.

### 3.3. Later Accretion Phase – Mean Energies

The directionally averaged neutrino mean energies show an almost monotonic rise. The infall of composition interfaces, however, can lead to short phases of stagnation or even drops in the mean energies, but the mean energies are much less affected by changes in the accretion rate than the luminosities.

In all but the two least massive progenitors (u8.1 and z9.6), we eventually observe a crossing of the mean energies of electron antineutrinos and heavy flavor neutrinos, and hence a violation of the canonical hierarchy of mean energies  $\langle E_{\nu_{\mu/\tau}} \rangle > \langle E_{\bar{\nu}_e} \rangle > \langle E_{\nu_e} \rangle$ . This feature has been found by many modern 1D and 2D neutrino-hydrodynamics simulations (Liebendörfer et al. 2004; Marek et al. 2009; Marek & Janka 2009) that include some or all of the relevant thermal equilibration processes for heavy flavor neutrinos (neutrino-electron scattering, nucleon bremsstrahlung, neutrino pair conversion, energy-exchanges in neutrino-nucleon scattering reactions).

These processes are one important cause for the crossing as they push the effective heavy flavor temperature  $T_{\nu_{\mu/\tau}, \text{eff}} \approx \langle E_{\nu_{\mu/\tau}} \rangle / 3.15$  down close to the matter temperature in the roughly isothermal atmosphere of the proto-neutron star (where most of the electron neutrinos and antineutrinos are produced prior to the explosion), a process discussed at length in Raffelt (2001); Keil et al. (2003). However, this does not yet account for the crossing of the mean energies, which hinges on two other factors that are illustrated in Figure 7. Figure 7 shows the evolution of the mean flux temperature  $T_{\text{flux}}$  and the local spectral temperature  $T_{\nu, \text{loc}}$  of the different neutrino species as they propagate out of the proto-neutron star atmosphere compared to the matter temperature at a time well after the crossing for model s25. The flux temperature

$T_{\text{flux}}$  for species  $i$  is defined in terms of the 1st angular moment  $H$  of the energy-dependent neutrino intensity in the comoving frame as

$$T_{\text{flux}} = \frac{1}{3.15} \frac{\int_0^\infty H dE_\nu}{\int_0^\infty E_\nu^{-1} H dE_\nu}, \quad (6)$$

i.e. the temperature  $T_{\text{flux}}$  is obtained from ratio of the neutrino energy and number flux assuming that the spectrum is a Fermi-Dirac spectrum with vanishing chemical potential. The local neutrino temperature  $T_{\nu, \text{loc}}$  is defined similarly in terms of the 0th moment  $J$  as

$$T_{\nu, \text{loc}} = \frac{1}{3.15} \frac{\int_0^\infty J dE_\nu}{\int_0^\infty E_\nu^{-1} J dE_\nu}. \quad (7)$$

$T_{\text{flux}}$  reflects the thermodynamic conditions in the decoupling region, and with a negative temperature gradient in the outer neutron star atmosphere one could naturally expect the standard hierarchy, since the heavy flavor neutrinos decouple at smaller radii than electron antineutrinos.

However, Figure 7 demonstrates a loophole in this argument. As already pointed out by Liebendörfer et al. (2004), a *temperature inversion* can occur in the cooling region, where  $\nu_e$  and  $\bar{\nu}_e$  are produced by charged-current processes. The flux temperature of electron antineutrinos can therefore be higher than that of the heavy flavor neutrinos. The asymptotic value of  $T_{\bar{\nu}_e, \text{flux}}$  roughly corresponds to the local temperature maximum at  $\sim 22$  km, whereas the flux temperature of  $\nu_{\mu/\tau}$ 's reaches its asymptotic value around the local temperature minimum at  $\sim 20$  km, which is about 0.5 MeV lower. The temperature inversion can easily be accounted for; it is a result of the competition between neutrino cooling and adiabatic compression in the accretion layer. Assuming spherical symmetry, stationarity, and Newtonian gravity, and neglecting self-gravity we can write the energy equation for the fluid in terms of the radial velocity  $v_r$ , the specific enthalpy  $h$ , the gravitational potential  $\Phi$ , and the source term  $\dot{q}$  due to neutrino heating/cooling as

$$\frac{d(h + \Phi)}{dt} = v_r \frac{\partial(h + \Phi)}{\partial r} = \frac{\dot{q}}{\rho}. \quad (8)$$

With baryon-dominated gas in the cooling region, the specific enthalpy is approximately  $5/2 k_b T / m_n$  ( $m_n$  being the nucleon mass) so that the gradient of  $h$  immediately reflects the temperature gradient, and the competition between cooling and adiabatic compression becomes obvious (note that both  $\dot{q}$  and  $v_r$  are negative in the cooling region):

$$\frac{5k_b}{2m_n} \frac{\partial T}{\partial r} \sim \frac{\dot{q}}{v_r} - \frac{\partial \Phi}{\partial r}. \quad (9)$$

As the density gradient in the atmosphere steepens, the accreted matter has to radiate away its gravitational binding energy while traversing an increasingly narrower cooling region. The balance is then tilted in favor of the term  $\frac{\dot{q}}{v_r}$  in Equation (9), and a positive temperature gradient in the outer proto-neutron star atmosphere arises.

Moreover, electron (anti)neutrinos of different energies decouple at different radii because the absorption and scattering cross sections scale with the square of the neutrino energy,  $E_\nu^2$ . The emerging energy-dependent luminosity  $dL/dE_\nu$  is essentially determined by the equilibrium intensity  $\mathcal{I}_{\text{eq}}$  at an optical



depth of  $\sim 2/3$  and by the effective emitting surface,

$$\frac{dL}{dE_\nu} \propto r(\tau = 2/3)^2 \times I_{\text{eq}}(\tau = 3/2, E_\nu). \quad (10)$$

Because of the relatively strong variation of  $I_{\text{eq}}$  with temperature  $I_{\text{eq}} \propto E_\nu^3 [1 + \exp(E_\nu/k_b T - \eta_{\text{eq}})]$ , the emission of neutrinos with energies near the spectral maximum in the region around the local temperature maximum is enhanced compared to that of low-energy neutrinos that decouple further inside and thus at lower temperatures. As a result, the mean energy of the emerging non-thermal spectrum can be even higher than one would assume based on the temperature in the decoupling region (cf. Figure 7, lower panel).

Neutrinos in the high-energy tail, on the other hand, are emitted from regions where there is again an appreciable negative temperature gradient, and the spectrum therefore declines faster than a thermal spectrum for neutrinos well above the average energy. If the temperature inversion in the accretion layer is strong, this “pinching” (Janka & Hillebrandt 1989a,b; Raffelt 2001; Keil et al. 2003; Tamborra et al. 2012) is no longer effective enough to keep the electron antineutrino mean energy below that of the heavy flavor neutrinos during the late accretion phase. The root mean square energy,  $\langle E_\nu^2 \rangle^{1/2}$ , however, is more affected by the high-energy tail and always shows the canonical hierarchy  $\langle E_{\nu_e}^2 \rangle^{1/2} < \langle E_{\bar{\nu}_e}^2 \rangle^{1/2} < \langle E_{\nu_{\mu/\tau}}^2 \rangle^{1/2}$  (cf. also Marek & Janka 2009).

We should also mention that the precise instant of the crossing is probably affected by weak magnetism corrections (Horowitz 2002), which are different for  $\nu_{\mu/\tau}$  and  $\bar{\nu}_{\mu/\tau}$ . Weak magnetism lowers the opacity for antineutrinos and leads to somewhat harder spectra (by about 1 MeV; Liebendörfer et al. 2003; Bruenn et al. 2013), and this effect would also occur in  $\bar{\nu}_\mu$  and  $\bar{\nu}_\tau$ . The VERTEX transport code does not distinguish heavy flavor neutrinos and antineutrinos in its current implementation, so that we obtain mean energies for  $\bar{\nu}_{\mu/\tau}$  that are slightly too low. However, simulations that treat heavy flavor neutrinos and antineutrinos separately still show the crossing despite slightly higher heavy flavor antineutrino mean energies, albeit at slightly different times for  $\nu_{\mu/\tau}$  and  $\bar{\nu}_{\mu/\tau}$ .

### 3.4. Relation of Neutrino Mean Energies and Proto-Neutron Star Parameters

The gradual rise of the neutrino mean energies is clearly a consequence of the contraction of the proto-neutron star and its rising surface temperature. Surprisingly, little attention has been paid to the dominant parameters regulating the neutrinospheric temperature during the accretion phase so far. Figure 8 shows that for each model, the electron antineutrino mean energy scales remarkably well with the proto-neutron star mass  $M$  (defined by the baryonic mass contained in regions with densities exceeding  $10^{11} \text{ g cm}^{-3}$ ),

$$\langle E_{\bar{\nu}_e}(t) \rangle \propto M(t). \quad (11)$$

The transient stagnation or decrease of the mean energy associated with the infall of composition interfaces causes slight deviations from the relation. There is also a spread of  $\lesssim 20\%$  between different progenitor models such that more massive progenitors (s25 and s27) tend to have a somewhat lower ratio  $\langle E_{\bar{\nu}_e}(t) \rangle / M(t)$ . To first order, Equation (11) still accounts reasonably well for the large variation of the neutrino mean energies (11 MeV to 20 MeV for  $\bar{\nu}_e$ ) through the post-bounce phase for different progenitors.

How can this scaling be accounted for, and how can it be reconciled with the fact that the nuclear equation of state also affects the neutrino mean energies considerably (Sumiyoshi et al. 2005; Marek et al. 2009; Marek & Janka 2009; O’Connor & Ott 2013)? In order to answer this question, we construct a simple model for the isothermal atmosphere of the proto-neutron star whose properties determine the emerging electron neutrino and antineutrino spectrum.

We first note that the transition from a steep negative temperature gradient in the roughly isentropic accretion mantle of the proto-neutron star to an almost flat temperature gradient in the cooling region (Figure 7) roughly coincides with the neutrinosphere for  $\bar{\nu}_e$  (simply because efficient cooling can only occur at low optical depth  $\tau$ ). At the neutrinosphere radius  $R_\nu$ , we have

$$\tau = \int_{R_\nu}^{\infty} \kappa_{\text{eff}} dr \approx 1, \quad (12)$$

where  $\kappa_{\text{eff}}$  is the effective energy-averaged opacity for electron antineutrinos. Since the dominant absorption and scattering opacity scales with the density  $\rho$  and the neutrino energy  $E_\nu$  as  $\rho E_\nu^2$ , this implies

$$C \int_{R_\nu}^{\infty} \rho T_\nu^2 dr \approx 1, \quad (13)$$

where  $T_\nu$  is the temperature at the average neutrinosphere (and the effective temperature of the emitted electron antineutrinos), and  $C$  is a normalization constant. The density  $\rho(r)$  in this integral is in turn determined by the density  $\rho_\nu$  at the base of the roughly isothermal, baryon-dominated atmosphere (cooling region and neutrinospheric region), the temperature  $T_\nu$ , and the local gravitational acceleration  $GM/R_\nu^2$  at  $R_\nu$  (cp. Mihalas & Weibel Mihalas 1984, Chapter 2),

$$\rho \approx \rho_\nu \exp\left(-\frac{GM(r - R_\nu)m_n}{R_\nu^2 k T_\nu}\right). \quad (14)$$

Using these relations,<sup>1</sup> we can determine that the effective optical depth  $\tau_\nu$  for electron antineutrinos at the base of the atmosphere scales as

$$\tau_\nu \propto \frac{\rho_\nu R_\nu^2 T_\nu^3}{GM}. \quad (15)$$

$\rho_\nu$  can be eliminated from this relation if we bear in mind that for  $r < R_\nu$ , the stratification in the thick accretion mantle is roughly adiabatic because it is well-mixed by proto-neutron star convection. For densities sufficiently below nuclear saturation density and down to  $\rho_\nu$ , where the nearly isentropic mantle smoothly joins the isothermal atmosphere, the plasma can be described as a mixture of relativistic and non-relativistic ideal gas components, and the adiabaticity constraint therefore leads to a power-law for the temperature,

$$T = K(s)\rho^{\gamma-1}, \quad (16)$$

where  $\gamma \approx 3/2$  is the effective adiabatic index and  $K(s)$  is a constant depending solely on the entropy  $s$ . The specific entropy in the accretion mantle (and hence  $K(s)$ ) does not vary considerably across progenitors and changes very slowly during the accretion phase for the following reasons: The entropy profile during the early post-bounce phase is determined by

<sup>1</sup> Note that the integral in Equations (12), (13) is dominated by the contributions from regions close to the neutrinosphere where Equation (14) holds.

the shock propagation through the iron core, which is rather similar for different progenitors. During the subsequent post-bounce evolution, the matter piled up on the proto-neutron star surface then cools down to the bulk entropy of the accretion matter as it settles, and essentially just extends the accretion mantle with constant entropy. The rather high mass of the mantle and a thermal relaxation (cooling) time-scale on the order of seconds also help to keep the entropy relatively constant.

After eliminating  $\rho_\nu$ , the condition  $\tau_\nu \approx 1$  at the neutrinosphere translates into a relation between the neutrinosphere temperature and the surface gravity at the base of the atmosphere:

$$T_\nu^5 \propto \frac{GM}{R_\nu^2}. \quad (17)$$

The neutrinosphere radius  $R_\nu^2$  is essentially determined by the proto-neutron star mass only through the mass-radius relationship for neutron stars with a cold inner core ( $s \approx 1 \text{ k}_b/\text{nucleon}$ ) of  $\approx 0.43 \dots 0.5 M_\odot$  (depending on the EoS) and an adiabatically stratified mantle with  $s \approx 5 \text{ k}_b/\text{nucleon}$ .  $R_\nu$  is a relatively steep function of the proto-neutron star mass, in contrast to cold neutron stars, where  $R \approx \text{const.}$  over a wide range of masses for nucleonic EoSs (see, e.g., Figure 1 in Müller et al. 2012b for an example with a mantle of relatively low entropy). Indeed, the steepness of the mass-radius relation for cold neutron stars partly helps to understand why proto-neutron stars with a hot mantle contract strongly with increasing mass, as we shall see in the following.

In the core of a proto-neutron star above nuclear saturation density, repulsive nucleon-nucleon interactions dominate the pressure, and thermal effects are subdominant. Down to and even somewhat below nuclear saturation density, the density profile of the proto-neutron star therefore roughly follows a TOV solution for a cold neutron star. Somewhat below nuclear saturation density, the thermal pressure of the baryons becomes the dominant contribution, and the density profile transitions into the TOV solution for an adiabatic mantle, with a much more shallow decline of the density compared to cold neutron stars at comparable densities.

Since the density profile of cold neutron stars is very steep below saturation density, the “fitting radius” between the core and the mantle is always close to the radius of a cold neutron star with a baryonic mass identical to that of the core. The steepness of the mass-radius relation for cold neutron stars (Lattimer & Prakash 2007; Steiner et al. 2010) implies that the radius of the inner core remains roughly constant as the proto-neutron star accretes. This is illustrated in Figure 9, which shows the evolution of isosurfaces corresponding to nuclear saturation density and lower fiducial densities in the neutron star for model s25.

The outer radius of the adiabatic mantle on top of the core, i.e.  $R_\nu$ , not only depends on the radius of the inner core, but also on the gravitational acceleration in the mantle: The pressure at the base of the mantle,  $P_{\text{core}}$ , remains fairly constant as the proto-neutron star accretes; it is roughly given by the pressure of cold neutron star matter at the fitting density. As the proto-neutron star grows in mass and the surface gravity increases, only a more and more tenuous mantle can be supported by  $P_{\text{core}}$ , and therefore the mantle contracts. More quantitatively, we can argue that the extent of the mantle is regulated by the pressure scale-height  $\ell$ , which is inversely proportional to the mass of the supranuclear core  $M_{\text{core}}$ ,  $\ell \propto P_{\text{core}}/(M_{\text{core}}^{-1})$ . Since more and more of the proto-

neutron star mass is concentrated in the core as its total baryonic mass increases, and since the self-gravity of the mantle also plays a role,  $R_\nu$  actually declines even faster with  $M$  than  $M^{-1}$ . The rapid contraction of isosurfaces for densities of  $\sim 10^{11\dots 12} \text{ g cm}^{-3}$ , is also shown in Figure 9.

Of course, the precise dependence of  $R_\nu$  on  $M$  can only be determined by the solution of the TOV equation either for a pre-defined stratification or by using the dynamically evolving stratification in supernova simulations in conjunction with a solution of the stationary neutrino transport equations (which is both implicitly done as we evolve the models). Empirically, it turns out that well below the maximum neutron star mass, the solutions of the TOV equation (which is implicitly reproduced in our time-dependent simulations) for such a stratification can be approximated by a power law with index

$$\frac{d \ln R_\nu}{d \ln M} \sim -2, \quad (18)$$

as shown by Figure 9. This value for the power-law index suggests precisely the mass-temperature relation we find in our simulations,

$$T_\nu \propto M. \quad (19)$$

The actual TOV solution is, of course, *not* a power law. Nonetheless, deviations from this power-law behavior do not change the mass-temperature relation appreciably for two reasons: First, different power laws still give relatively similar neutron star radii simply because the proto-neutron star mass range is limited (cp. Figure 9). Furthermore, the high power of the temperature in Equation (17) implies that even a relative deviation of 30% between different power laws is reduced to a deviation of 11% in  $T_\nu$ .

Naturally, this mass-temperature relation is modified by slight progenitor variations, by the varying strength of the accretion effect described in Section 3.3, and by gravitational redshift. Progenitor variations in the mass-temperature relation can be traced to slightly different entropies in the proto-neutron star convection zone. Higher entropies in more massive progenitors (s25, s27) lead to somewhat lower neutrino mean energies.

The equation of state is another important factor that regulates the neutrino mean energies through the compactness of the proto-neutron star (Sumiyoshi et al. 2005; Marek et al. 2009; Marek & Janka 2009; O’Connor & Ott 2013). This is not inconsistent with the mass-temperature relation (19). Different equations of state will lead to different mass-radius relations for the core and mantle, and hence affect the surface gravity at the neutrinosphere. Stiffer equations of state generally result in a smaller core mass, a more massive and extended mantle, and hence somewhat smaller neutrinosphere temperatures. However, this affects only the proportionality constant in the mass-temperature relation (19). Since relativistic effects in the mantle are only of moderate magnitude and equation-of-state variations mainly change the radius of the core dominated by nucleon interactions, similar power-laws are expected for different equations of state as long as the core radius varies little with mass as suggested by neutron star radius measurements (Lattimer & Prakash 2007; Steiner et al. 2010). Even a different slope of the mass-radius relationship for proto-neutron stars with a hot accretion mantle does not strongly affect the relation expressed by Equation (19) because the neutrino temperature enters as  $T_\nu^5$  in the underlying relation (17). 1D simulations with the EoS of Shen et al. (1998) indeed show a similar scaling relation for the electron

antineutrino mean energy (Hüdepohl et al., in preparation).

### 3.5. The Explosion Phase

Different from artificial 1D explosion models, we find no clear fingerprint of shock revival in the angle-averaged neutrino luminosities and mean energies. Specifically, there is no abrupt drop in the electron neutrino and antineutrino luminosity associated with the onset of the explosion. Models where the shock moves out very rapidly and accretion is quenched rather abruptly (like u8.1 or z9.6) also have a rather low accretion luminosity to begin with so that a strong decline of the luminosity cannot be expected. For other progenitors (s11.2 and s27), the onset of the explosion is associated with a strong decline of the luminosity, but this is just a reflection of the infall of the shell interface that triggers shock revival. Moreover, the decline of the electron neutrino and antineutrino luminosity can also be rather gradual because much of the shocked material is still channeled down to the proto-neutron star through accretion downflows in these cases. In cases where the explosion is not associated with the infall of a shell interface (model s15s7b2), or where the accretion rate remains high (e.g. because of a strongly unipolar explosion geometry), there may even be no trace at all of shock revival in the total neutrino luminosity.

The angle-averaged mean energies of electron neutrinos and antineutrinos may show only weak fingerprint of shock revival: For models u8.1, z9.6, and s11.2, the mean energies stagnate or even decline slowly over extended periods ( $> 100$  ms), implying that there is almost no further accretion onto the proto-neutron star. However, there is still a considerable rise in the mean energies in models s15s7b2 and s27 due to the high mass accretion rates after shock revival.

In models s11.2 and s27, the explosion phase is characterized by stronger non-monotonic variations in the total luminosity and the angle-averaged mean energies than during the accretion phase. Such variations on intermediate time-scales are also associated with anisotropic neutrino emission and are discussed at length in Section 4.3

## 4. SPATIO-TEMPORAL VARIATIONS IN THE NEUTRINO EMISSION AND THE OBSERVABLE NEUTRINO SIGNALS

Nonradial instabilities like convection and the SASI as well as global asymmetries during the explosion phase lead to anisotropic neutrino emission. As a result, the observable neutrino luminosities and mean energies become strongly direction-dependent and deviate considerably from the directionally averaged luminosities and mean energies discussed in Section 3. In this Section, we analyze the time-frequency structure of the observable neutrino signal and elucidate how it can reveal detailed time-dependent information about the dynamics in the supernova core during the accretion and explosion phase.

### 4.1. Reconstruction of the Observable Neutrino Signal

Since the ray-by-ray-plus transport does not account for lateral neutrino flux components outside the neutrinosphere, the information on each “ray” for angle  $(\theta, \varphi)$  in 3D or latitude  $\theta$  in 2D can only propagate radially. In reality, an observer outside the neutrinosphere would receive flux not just from one angular zone (i.e. ray), but from the whole radiating surface facing him. The observable neutrino luminosity along a specific direction  $(\theta, \varphi)$  therefore differs from the asymptotic value of

the “ray luminosity”  $4\pi\alpha^2\phi^4 F_{\text{eul}}(r, \theta, \varphi)r^2$  for  $(r \rightarrow \infty)$  in the integrand of Equation (2). For this reason, we reconstruct the observable signal from the ray-dependent neutrino fluxes following the method of Müller et al. (2012c), which assumes a neutrinospheric emission law  $I(\mathbf{n}) \propto 1 + 3/2 \cos \gamma(\mathbf{n})$  for the neutrino intensity as a function of the angle  $\gamma$  between the radial direction and the direction vector  $\mathbf{n}$  of the emitted neutrinos. The observable luminosity  $L_o(\mathbf{n})$  at infinity along the direction  $\mathbf{n}$  is then given by the integral of  $I(\mathbf{n})$  over the visible emitting surface (surface elements  $dA$ ),

$$L_o(\mathbf{n}) = 2 \int_{\text{vis. surf.}} F_{\text{eul}}(\mathbf{r}, \theta) \left(1 + \frac{3}{2} \cos \gamma(\mathbf{n})\right) \cos \gamma(\mathbf{n}) dA. \quad (20)$$

Observable expectation values  $\langle E_o^i(\mathbf{n}) \rangle$  of powers of the neutrino energy  $E$  can be obtained in a similar manner from the first angular moment of the neutrino radiation intensity:

$$\langle E_o^i(\mathbf{n}) \rangle = \frac{\int_{\text{vis. surf.}} \int_0^\infty E^{i-1} H(E_\nu, \mathbf{r}, \theta) \left(1 + \frac{3}{2} \cos \gamma\right) \cos \gamma dE dA}{\int_{\text{vis. surf.}} \int_0^\infty E^{-1} H(E_\nu, \mathbf{r}, \theta) \left(1 + \frac{3}{2} \cos \gamma\right) \cos \gamma dE dA}. \quad (21)$$

In order to study the observability of temporal variations in the neutrino emission, we use  $L_o(\mathbf{n})$  and  $\langle E_o^i(\mathbf{n}) \rangle$  to estimate the expected signal in IceCube (Abbasi et al. 2011; Salathé et al. 2012), which is best suited for detecting fast time variations among operating detectors thanks to its excellent temporal resolution and to the prospective high event rate (cp. Lund et al. 2010, 2012; Tamborra et al. 2013). Since a simplified detector model is fully sufficient for the purpose of demonstration, we estimate the excess rate  $\mathfrak{R}$  per time bin ( $\Delta t = 1.6384$  ms) over the background due to supernova neutrinos following Halzen & Raffelt (2009):

$$\mathfrak{R} = 186 \text{ bin}^{-1} \frac{\tilde{L}_o}{10^{52} \text{ erg s}^{-1}} \frac{\langle \tilde{E}_o^3 \rangle \langle \tilde{E}_o \rangle}{225 \text{ MeV}^2} \left( \frac{10 \text{ kpc}}{d} \right)^2. \quad (22)$$

Here,  $\tilde{L}_o$ ,  $\tilde{E}_o^3$ , and  $\tilde{E}_o$  are the electron antineutrino luminosity and the third and first energy moment of the distribution function as measured on Earth, and  $d$  is the distance to the supernova. The background rate  $\mathfrak{R}_0$  is taken to be

$$\mathfrak{R}_0 = 2200 \text{ bin}^{-1}. \quad (23)$$

The luminosity  $\tilde{L}_o$  and the energy moments  $\langle \tilde{E}_o^i \rangle$  of electron antineutrinos emitted from the supernova may be modified by MSW resonances in the outer shells of the progenitor and by non-linear collective neutrino flavor conversion (see Duan & Kneller 2009; Duan et al. 2010 for a review). These effects partly depend on unknown neutrino parameters (mass hierarchy); and non-linear flavor conversion is not yet completely understood, in particular in the absence of axial symmetry in the radiation field (Mirizzi 2013; Raffelt et al. 2013). As a full exploration of the possible scenarios is beyond the scope of this paper, we estimate the IceCube signal under the optimistic assumption of a normal mass hierarchy and neglect non-linear flavor conversion (which is probably suppressed until the later neutrino-driven wind phase, see Chakraborty et al. 2011; Sarikas et al. 2012a,b). Furthermore, we neglect any possible reconversion of neutrinos due to the Earth effect. Under these assumptions, the observable electron antineutrino luminosity and the energy moments relevant

for the IceCube signal can be expressed in terms of the unmodified quantities  $L_o$ ,  $\langle E_o \rangle$  and  $\langle E_o^3 \rangle$  (cp. Kachelrieß et al. 2005)

$$\tilde{L}_o = \cos^2 \theta_{12} L_{o,\bar{\nu}_e} + \sin^2 \theta_{12} L_{o,\bar{\nu}_\mu}, \quad (24)$$

$$\tilde{E}_o = \cos^2 \theta_{12} \langle E_{o,\bar{\nu}_e} \rangle + \sin^2 \theta_{12} \langle E_{o,\bar{\nu}_\mu} \rangle, \quad (25)$$

$$\tilde{E}_o^3 = \cos^2 \theta_{12} \langle E_{o,\bar{\nu}_e}^3 \rangle + \sin^2 \theta_{12} \langle E_{o,\bar{\nu}_\mu}^3 \rangle, \quad (26)$$

where  $\sin^2 \theta_{12} = 0.311$  (Beringer et al. 2012). While we cannot hope to discuss the possible impact of flavor conversion on our findings in its entirety, this simplified approach at least reflects the fact that detectors will never measure the unoscillated  $\bar{\nu}_e$  signal computed in our simulations. Using the unoscillated neutrino flux would result in a systematic overestimation of the signal-to-noise ratio of features in the time-frequency domain. Our simplified flavor conversion is intended to roughly represent the most optimistic case (maximum amplitude of fluctuations in the observed electron antineutrino flux) that can possibly be encountered.

The actual detector signal will also be subject to statistical fluctuations. We therefore compute simulated IceCube signals assuming a Poisson distribution with an expectation value of  $\mathcal{R}(t)$  in each bin. Such simulated signals for the four progenitor models s11.2, s15s7b2, s25, and s27 for observers located in the north and south polar directions and in the equatorial plane are shown in Figure 10. The assumed distance is  $d = 10$  kpc, except for model s11.2 ( $d = 5$  kpc). As the low-mass progenitors u8.1 and z9.6 do not exhibit pronounced spatio-temporal variations in the neutrino emission, we do not discuss these models any further in this section.

Different from earlier work on the subject (Marek & Janka 2009; Lund et al. 2010; Brandt et al. 2011; Lund et al. 2012; Tamborra et al. 2013), we not only study the frequency spectrum for the entire signal or distinct phases of the evolution, but instead analyze the full time-frequency structure of the expected IceCube signals by means of a wavelet analysis. The wavelet transform  $\chi(t, p)$  of the rate  $\mathcal{R}$  depends both on time  $t$  and on the period  $p$ , and is given in terms of the mother wavelet  $\psi$  by

$$\chi(t, p) = \frac{1}{\sqrt{|p|}} \int_{-\infty}^{\infty} (\mathcal{R}(t) + \mathcal{R}_0) \psi^* \left( \frac{t' - t}{p} \right) dt'. \quad (27)$$

For evaluating Equation (27), we use the discrete Poisson realization of the binned IceCube data (including the background), and we employ the Morlet wavelet as mother wavelet with a scaling parameter<sup>2</sup>  $\sigma = 6$ :

$$\psi(x) = \left( 1 + e^{-\sigma^2} - 2e^{-3\sigma^2/4} \right)^{-1/2} \pi^{-1/4} e^{-x^2/2} \times \left( e^{i\sigma x} - e^{-\sigma^2/2} \right). \quad (28)$$

In order to assess the significance of features in the wavelet spectrogram, we consider the squared signal-to-noise ratio  $(S/N)^2$  between the absolute square of the wavelet transform and the expectation value  $\langle |\chi_{\text{noise}}|^2 \rangle$  due to the background,

$$(S/N)^2 = \frac{|\chi|^2(t, p)}{\langle |\chi_{\text{noise}}|^2 \rangle}. \quad (29)$$

<sup>2</sup> The scaling parameter determines the width of the wavelet in terms of the wavelength. We opt for a relatively small value to achieve better temporal resolution.

The computation of  $\langle |\chi_{\text{noise}}|^2 \rangle$  for Poissonian noise in different time bins is described in the Appendix. For the discrete wavelet transform,  $\langle |\chi_{\text{noise}}|^2 \rangle$  depends weakly on the period  $p$  as long as  $p \gg \Delta t$  and  $p \ll T$  (where  $T$  is length of the time series). To avoid spuriously high signal-to-noise ratios for  $p \approx \Delta t$ , we always use the noise level at  $p \approx 50$  ms.

Wavelet spectrograms showing  $(S/N)^2$  for some observer directions and different distances are shown in Figures 11, 12 (s25), 13 (s15s7b2), 14 (s11.2) and 15 (s27).

The simulated real-time signals in Figure 10 show clearly discernible temporal variations on top of the secular evolution that we already discussed for the total angle-averaged luminosity. The wavelet spectrograms reveal that these variations are indeed caused by spatio-temporal modulations in the emission and not by white noise due the detector background. It is convenient to analyze the distinct fingerprints of the pre-explosion phase and the explosion phase separately.

#### 4.2. Signatures of SASI Oscillations

The most remarkable feature of neutrino emission in the pre-explosion phase is seen in strongly SASI-dominated models like s25 and s27 (bottom panels of Figure 10), which exhibit a strong quasi-periodic modulation of the signal for observers located along the direction of the SASI sloshing motions (Marek & Janka 2009; Ott et al. 2008; Brandt et al. 2011; Lund et al. 2010, 2012; Tamborra et al. 2013). In a model like s15s7b2 (top right panel of Figure 10), in which the SASI is probably present but where strong convective overturn also develops, such modulations are still visible but far less pronounced. The modulations are particularly strong for a model like s25 that either fails to explode or would eventually explode at very late times.

In such a case, SASI activity may persist over several hundreds of milliseconds with little activity of parasitic instabilities on top of the SASI, and thus with a well-defined periodicity of the oscillations. This gives rise to a distinct pattern in the wavelet spectrograms (Figures 11 and 12) that shows a continuous decrease of the SASI period as the shock retracts. This decrease may be interrupted by sudden drops in the accretion rate associated with the infall of a composition shell interface in the progenitor. The changing conditions when such an interface falls through the shock cause a transient interruption of the quasi-periodic shock oscillations (Figure 11). In the case of model s25, the drop in the accretion rate is clearly reflected in the time-dependent neutrino signal (bottom left panel of Figure 10). If SASI activity resumes afterward, it may do so with a somewhat longer oscillation period than before, which is reflected as a small step in the frequency band in the bottom right panel of Figure 11.

The SASI-induced modulations of the neutrino emission are most pronounced for observers located along the direction of SASI sloshing, but even for observers viewing the supernova from an orthogonal direction, the time-frequency structure of the neutrino signal still shows fingerprints of SASI activity (top right panel of Figure 11), in particular if we assume a distance smaller than 10 kpc, as shown by the spectrograms in Figure 12. However, the frequency appears to be much broader in this case, reaching to significantly lower periods. The bottom panel of Figure 12 (which shows the spectrogram for an observer in the equatorial plane at 2 kpc) suggests that there may be two emission bands and that the dominant modulation frequency is roughly twice as large as for a polar observer. This is just a reflection of the fact that an excursion of the shock in either direction will affect the

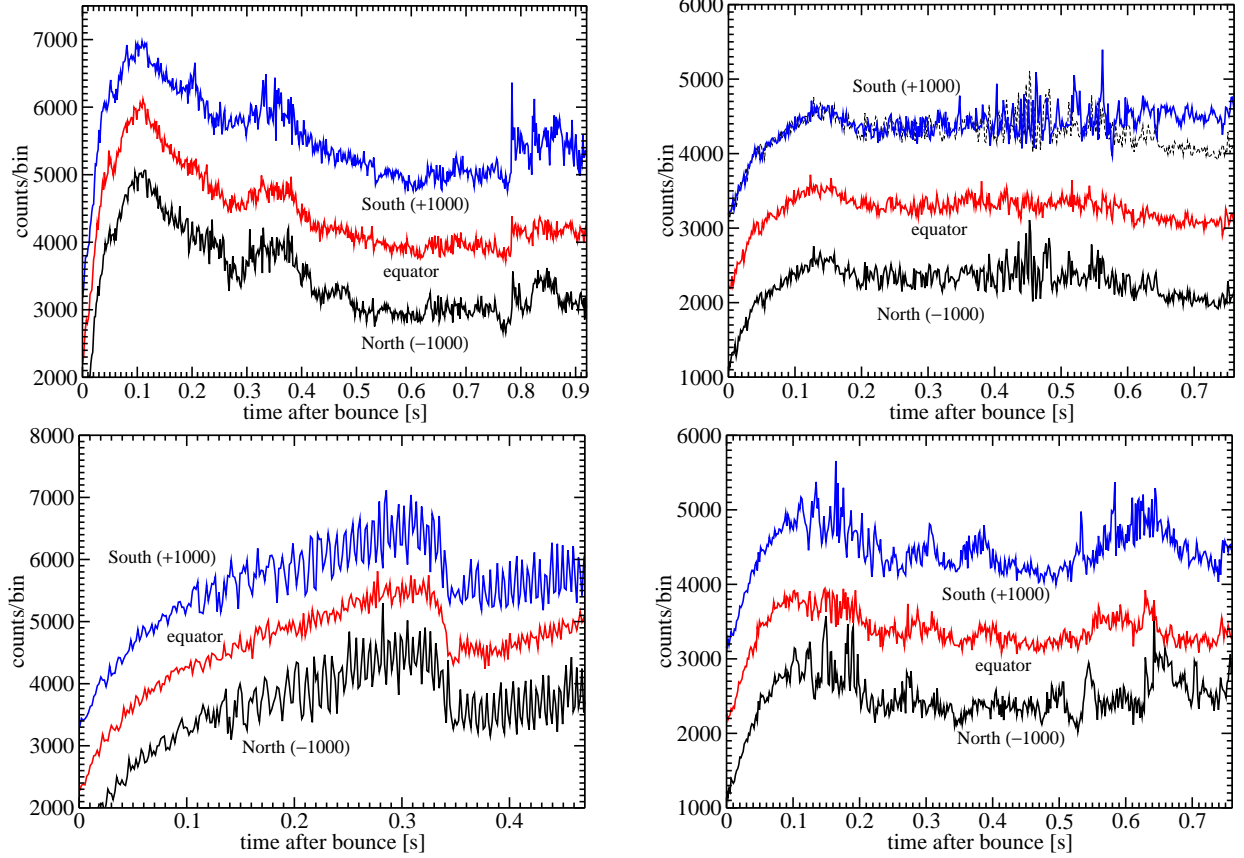


**Figure 10.** Simulated IceCube signals (including background) for models s11.2 (top left, at 5 kpc), s15s7b2 (top right, at 10 kpc), s25 (bottom left, at 10 kpc), and s27 (bottom right, at 10 kpc) for observers situated in the north/south polar directions and in the equatorial plane. Note that we use an offset of  $\pm 1000$  for polar observers to avoid overlapping curves. For model s15s7b2 (top right panel), the count rate in the equatorial plane is shown as dashed black line with an offset of +1000 to illustrate the enhanced emission in the southern hemisphere due to the asymmetric explosion geometry.

neutrino emission in the equatorial plane in the same manner. For a real detection, the relative orientation of the observer to a putative sloshing mode of the SASI would be unknown, but the presence or absence of a secondary emission peak at lower frequencies (longer periods) would allow a discrimination between the “real” SASI frequency band and the artificial “overtone” that occurs for an observer not located along the direction of the sloshing mode. For a pure spiral mode, this overtone would probably be absent, and the viewing angle would only affect the amplitude of the modulations.

The IceCube signal from a Galactic supernova could thus not only provide unambiguous evidence about SASI activity in the supernova core, but might even give some hints about the involved modes (sloshing vs. spiral modes) and could allow us to directly follow the temporal evolution of the SASI frequency. This would also provide qualitative information about the shock radius and the proto-neutron star radius, which set the oscillation period of the SASI (Foglizzo et al. 2007; Scheck et al. 2008). Quite remarkably, it is possible to formulate a rather simple quantitative relation between the time-dependent period of the IceCube signal modulations and these two radii. If the SASI is due to an advective-acoustic cycle, its period is given by the sum of the advective and acoustic time-scales for perturbations traveling between the (angle-averaged) shock radius  $r_{\text{sh}}$  and the radius of maximum deceleration  $r_{\text{v}}$  (Foglizzo et al. 2007; Scheck et al. 2008):

$$T_{\text{SASI}} = \tau_{\text{adv}} + \tau_{\text{ac}} = \int_{r_{\text{v}}}^{r_{\text{sh}}} \frac{dr}{|v_r|} + \int_{r_{\text{v}}}^{r_{\text{sh}}} \frac{dr}{c_s - |v_r|}. \quad (30)$$

Here,  $v_r$  and  $c_s$  are the (average) radial velocity and the local sound speed. The velocity profile between  $r_{\text{sh}}$  and  $r_{\text{v}}$  is roughly linear,

$$v_r \sim -\beta^{-1} \sqrt{\frac{GM}{r_{\text{sh}}}} \left( \frac{r}{r_{\text{sh}}} \right), \quad (31)$$

where  $\beta$  is the ratio between the post-shock and pre-shock density. Since the flow becomes very subsonic close to  $r_{\text{v}}$ , the advection time-scale  $\tau_{\text{adv}}$  will typically be the dominant term that decides about the scaling of  $T_{\text{SASI}}$  with the parameters of the accretion flow ( $M$ ,  $r_{\text{sh}}$ ,  $r_{\text{v}}$ ). Plugging in Equation (31) into Equation (30) and neglecting the acoustic time-scale results in

$$T_{\text{SASI}} \propto r_{\text{sh}}^{3/2} M^{-1/2} \ln \left( \frac{r_{\text{sh}}}{r_{\text{v}}} \right). \quad (32)$$

The radius of maximum deceleration  $r_{\text{v}}$  is somewhat difficult to infer from simulations, and its dependence on other proto-neutron star parameters (mass, core radius  $R_{\text{core}}$ , neutrinosphere radius, gain radius, surface temperature) is rather complicated since the location of the coupling region for vorticity perturbations and acoustic perturbations also depends on the density gradient in the cooling region (Scheck et al. 2008). However, we can formulate an empirical scaling law in terms of the proto-neutron star radius  $r_{\text{PNS}}$  (defined by a fiducial density of  $10^{11} \text{ g cm}^{-3}$  as in Müller et al. 2012b; Bruenn et al. 2013; Suwa et al. 2013) for the SASI oscillation

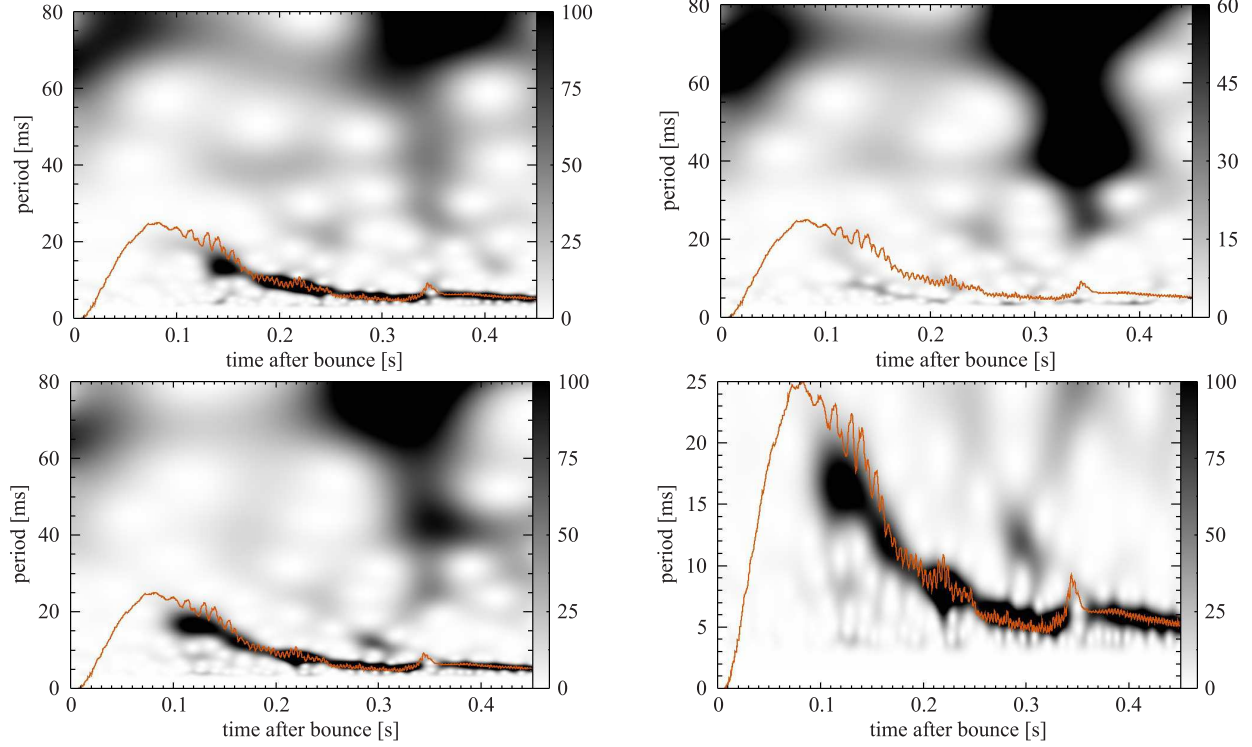


**Figure 11.** Wavelet spectrograms of simulated IceCube signals for model s25 for observers situated at a distance of 10 kpc in the north polar direction (top left panel), in the equatorial plane (top right panel), and along the south polar axis (bottom panels). The SASI period predicted by Equation (33) is shown as a red curve in each panel. The colorbar shows the scale for the signal-to-noise ratio computed according to Equation (29).

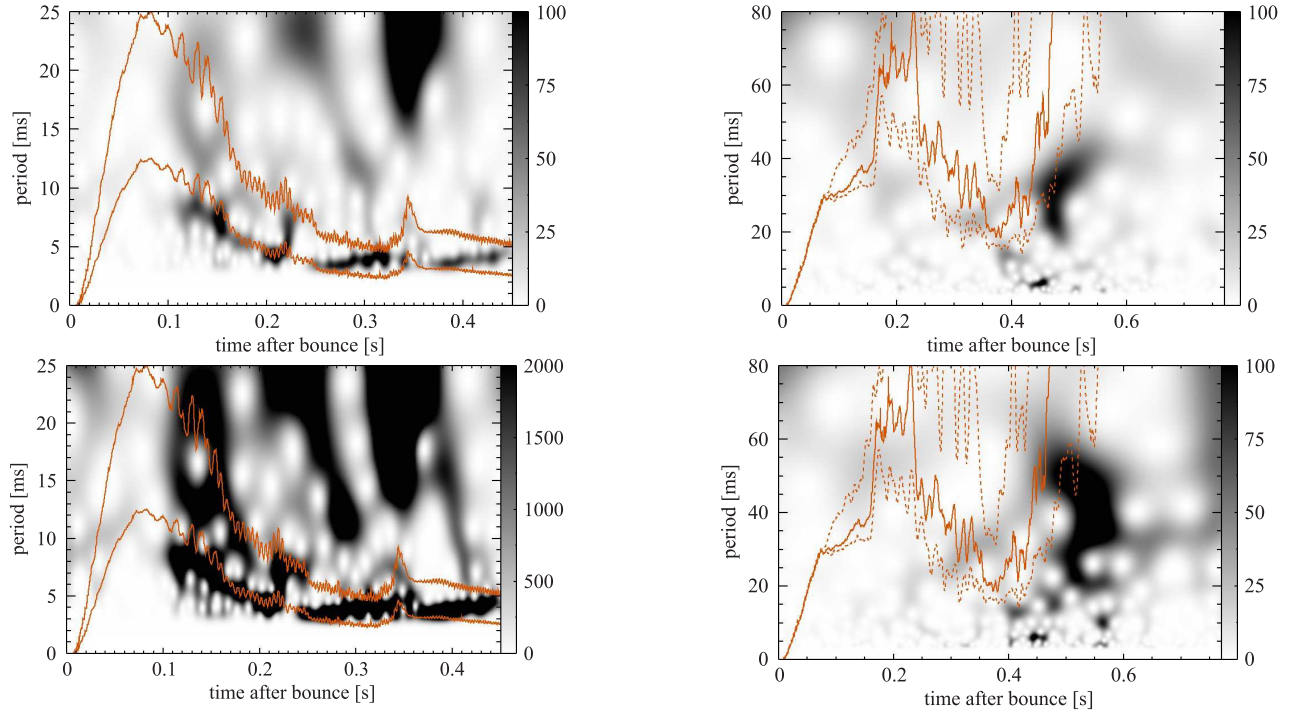


**Figure 12.** Wavelet spectrograms of simulated IceCube signals for model s25 for observers situated in the equatorial plane at a distance of 5 kpc (top panel) and 2 kpc (bottom panel). The grayscale indicates the squared signal-to-noise ratio  $(S/N)^2$  (Equation 29). Red curves show the predicted values of  $T_{\text{SASI}}$  and  $T_{\text{SASI}}/2$  according to Equation (33). The colorbar shows the scale for the signal-to-noise ratio computed according to Equation (29).

**Figure 13.** Wavelet spectrograms of simulated IceCube signals for model s15s7b2 for observers situated at a distance of 10 kpc in the north polar direction (top panel) and the south polar direction (lower panel). The SASI period predicted by Equation (33) is shown as a red curve in each panel. The dashed red lines show the estimates based on the maximum and minimum shock radius. The colorbar shows the scale for the signal-to-noise ratio computed according to Equation (29).



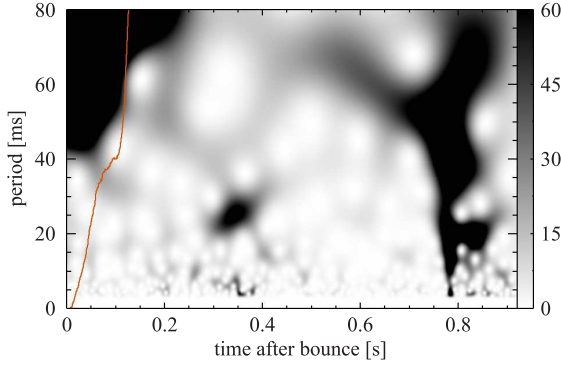


**Figure 14.** Wavelet spectrogram of the simulated IceCube signal for an observer in the south polar direction at 5 kpc for model s11.2. The SASI period predicted by Equation (33) is shown as a red curve. Note the stripe-like patterns indicating the formation of a new downflow onto the proto-neutron star around 800 ms and also around 350 ms. The colorbar shows the scale for the signal-to-noise ratio computed according to Equation (29).

period:

$$T_{\text{SASI}} = 19 \text{ ms} \left( \frac{r_{\text{sh}}}{100 \text{ km}} \right)^{3/2} \ln \left( \frac{r_{\text{sh}}}{r_{\text{PNS}}} \right). \quad (33)$$

Here, we have ignored the relatively weak dependence on  $M$  in Equation (32), which gives a somewhat better fit to the observed SASI periods when using  $r_{\text{PNS}}$  instead of  $r_{\text{V}}$  to estimate the advection time-scale. The prediction for  $T_{\text{SASI}}$  is indicated in Figures 11, 13, 14 and 15 by a red curve. In Figure 12,  $T_{\text{SASI}}/2$  is also shown.

While Figures 11 and 12 demonstrate that Equation (33) describes models with continuous SASI activity very well, one should also note that the models s15s7b2 (Figure 13) and s27 (Figure 15) show some activity around the expected frequency during the phases where the SASI is active (prior to the onset of the explosion at  $\sim 125$  ms in s27) and during the phase of strong shock retraction around 300...350 ms in s15s7b2). Even the supposedly convective model s11.2 (Figure 14) shows some (faint) broadband activity around the SASI frequency prior to the onset of the explosion (at  $p \approx 35$  ms at a post-bounce time of  $\approx 100$  ms). Among these exploding models with somewhat less extended and less regular SASI activity than model s25, model s27 is particularly noteworthy as it shows clear signs of an *increasing* shock oscillation period – and hence an increasing shock radius – from 100 ms onward. This is one of the characteristic features of exploding models, which we discuss in the following section.

However, different from a model like s25, the time-frequency structure of the neutrino signal of these models is a less robust indicator for SASI as the physical mechanism underlying the emission modulation. The broadband nature, the intermittent character of the signal modulations, and the temporal variability of the dominant frequency point to a significant and perhaps dominant role of convection in models like s15s7b2 and s11.2.

#### 4.3. Signatures of the Explosion Phase

As discussed in Section 3.5, the directionally averaged neutrino fluxes cannot serve as robust indicators for the onset of the explosion. The relatively abrupt decline of the luminosity seen in artificial 1D explosion models is often absent in multi-D simulations. A step-like decline in the electron neutrino and antineutrino luminosities rather points to the infall of a composition interface.

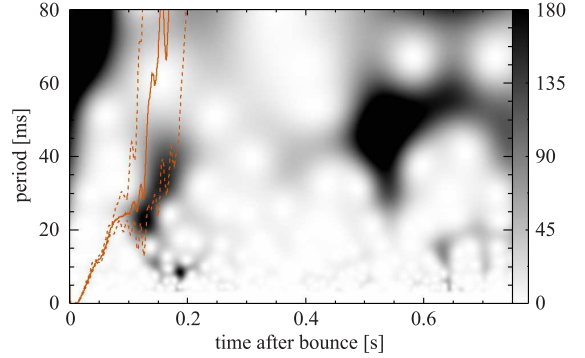


**Figure 15.** Wavelet spectrogram of the simulated IceCube signal for an observer in the north polar direction at 10 kpc for model s27. The SASI period predicted by Equation (33) is shown as a red curve. The dashed red lines show the estimates based on the maximum and minimum shock radius. The spectrogram reveals enhanced post-explosion accretion onto the proto-neutron star around 550 ms, 650 ms, and 720 ms. The colorbar shows the scale for the signal-to-noise ratio computed according to Equation (29).

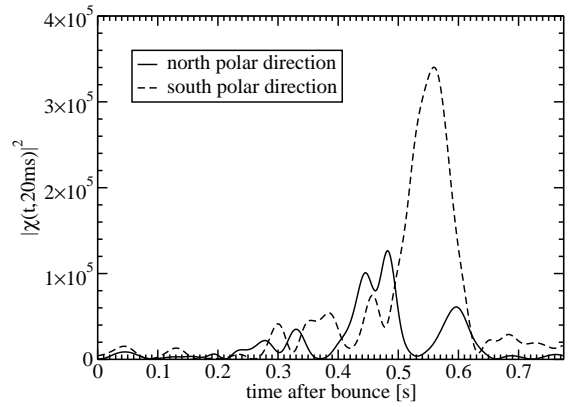


**Figure 16.** Squared absolute wavelet amplitude  $|\chi|^2$  for a period of 20 ms for model s15s7b2. The solid and dashed lines show  $|\chi|^2$  for observers situated along the north and south polar directions, respectively.

Fortunately, the spatio-temporal variations of the neutrino-emission provide several clues for diagnosing the transition from the accretion phase to the explosion phase. However, these fingerprints are not immediately obvious from a superficial visual inspection of the simulated IceCube detection rates in Figure 10. Fluctuations in the observable neutrino signal are present both prior to and after shock revival, and the amplitudes in both phases are not dissimilar. The occurrence of sustained *global* emission anisotropies (e.g. in model s15s7b2, top right panel of Figure 10) is a qualitative difference to the pre-explosion phase. Such global anisotropies can result from one-sided accretion in very asymmetric explosions (cf. our discussion of model s15s7b2 in Müller et al. 2012b), but they can obviously not be observed directly.

Nevertheless, the transition to the explosion betrays itself by quantitative and qualitative changes in the fluctuating neutrino signal: Due to the expansion of the shock, the typical frequency of the fluctuations decreases (Figures 13 and 15), and the fluctuations lack the well-defined periodicity familiar from SASI-dominated models in the pre-explosion phase. In the wavelet spectrograms of the exploding models s11.2, s15s7b2 and s27 (intermittent) broadband activity for periods longer than  $\gtrsim 20$  ms therefore dominates over short-period fluctuations. In our models, a typical period of fluctuations around  $\sim 20 \dots 25$  ms seems to provide a very rough dividing line between non-exploding and exploding models. Fig-



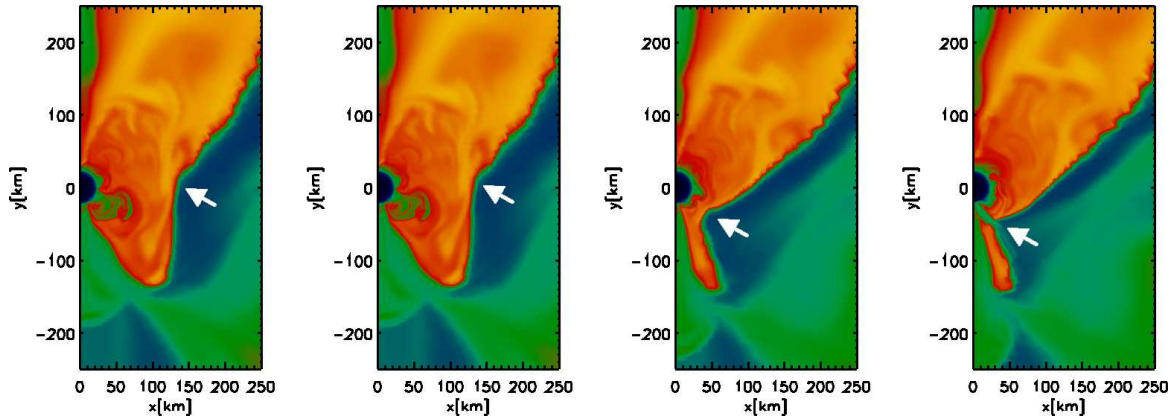


**Figure 17.** Snapshots of the entropy  $s$  (ranging from  $0k_B/\text{nucleon}$  (black) to  $35k_B/\text{nucleon}$  (yellow)) in the region around the proto-neutron star at post-bounce times of 812.3 ms, 816.5 ms, 819.7 ms, and 821 ms. The white arrow indicates where cold infalling material penetrates into the hot high-entropy bubble and eventually forms a new downflow, which then supplies fresh material to the cooling region and causes a small, burst-like enhancement of the neutrino emission.

ure 16 illustrates that for model s15s7b2 the activity peak at  $p = 20$  ms coincides very well with the phase of shock revival. *A neutrino signal dominated by fluctuations in the range of 40...50 Hz is therefore probably a good indicator for shock revival.*

It is worth noting that even during the phase of shock revival, the spectrum of the emission fluctuations still shows a preferred frequency at least in some models, albeit that the peak is rather broad. Model s15s7b2, for example, shows strong signal fluctuations around 500 ms for an observer along the north polar axis. The typical period of these fluctuations is in rough agreement with the advection time-scale between the *minimum* shock radius and the proto-neutron star (Figure 13 and also Figure 15 for the corresponding feature in model s27). This could suggest that some advective-acoustic feedback mechanism (which may or may not be identified with the SASI) is still active at this stage and provides a preferred time-scale for variations in the accretion flow and the neutrino emission.

Early fallback of some of the shocked material onto the proto-neutron star also gives rise to characteristic signatures in the neutrino emission after the onset of the explosion, for which model s11.2 is a prime example. As already discussed in Müller et al. (2012b, 2013), the energy of the hot, neutrino-heated material is relatively low in this case so that the high-entropy bubbles fail to push out all the material swept up by the shock after the onset of the explosion. Much of the shocked material is therefore channeled onto the proto-neutron star through long-lived downflows, but on occasion, some of the swept-up material also penetrates the expanding high-entropy bubbles to form a new downflow as illustrated in Figure 17. Such a new downflow not only excites oscillations of the proto-neutron star surface that give rise to burst-like gravitational wave emission (Müller et al. 2013), but also carries fresh material into the cooling region.

This results in a sudden jump in the neutrino emission, which would be observable by IceCube for a Galactic supernova at a distance of 5 kpc as can be seen in the top left panel of Figure 10 (with two prominent bursts at  $\sim 780$  ms and  $\sim 820$  ms). Although the mini-bursts in the neutrino-emission are more strongly pronounced for an observer in the south polar direction (i.e. above the hemisphere where the downflow develops), they are visible from any direction as the newly injected material is quickly redistributed across the whole cooling region. As the expected count rate rises by several hun-

dred, these events are clearly distinguishable from statistical fluctuations in the signal, which are of the order of  $\sqrt{N} \approx 63$  during the relevant phase. If the jump in the detection rate is statistically significant, such mini-bursts also leave a distinct trace in the wavelet spectrogram in the form of extended vertical stripes. These patterns are most clearly visible in the case of model s11.2 (Figure 14). Model s27 also shows such mini-bursts, albeit a little less sharp (Figure 15), e.g. at  $\sim 550$  ms and  $\sim 650$  ms. The detection of such signatures would not only indicate that an explosion has been initiated prior to the burst, but would also indicate that the explosion is (still) reasonably weak at this stage such that outflow and accretion downflows persist simultaneously for an extended period of time.

## 5. SUMMARY AND CONCLUSIONS

Based on six general relativistic 2D simulations of progenitors between  $8.1M_\odot$  and  $27M_\odot$ , we presented a detailed analysis of the neutrino emission from core-collapse supernovae from the bounce to the explosion phase. We discussed both the secular evolution of the total, angle-integrated neutrino emission, which is largely regulated by the continuous accretion of material and the contraction of the proto-neutron star, as well as spatio-temporal variations in the neutrino emission caused by nonaspherical hydrodynamic instabilities like convection and the SASI. Using simulated signals of a future Galactic supernova in IceCube (Abbasi et al. 2011; Salathé et al. 2012), we studied the observability of these spatio-temporal variations and showed how detailed information about the supernova core could be extracted from the observed neutrino signal by means of a time-frequency analysis.

Our most salient findings can be summarized as follows:

1. Prior to the onset of the explosion, the evolution of the total neutrino flux and the neutrino mean energies is in qualitative agreement with recent 1D models of the accretion phase (Liebendörfer et al. 2003, 2004; Buras et al. 2006a; Marek & Janka 2009; Fischer et al. 2009; O'Connor & Ott 2013) although proto-neutron star convection affects the neutrino emission on the level of 10...20% (Buras et al. 2006a). Similar to other modern neutrino hydrodynamics simulations, and in stark contrast to some earlier 1D models from the 1980's and 1990's, our 2D models are characterized

by very similar mean energies of electron antineutrinos and  $\mu/\tau$  neutrinos. In all but the least massive progenitors ( $8.1M_\odot$  and  $9.6M_\odot$ ), we even observe a crossing of the mean energies already within the first few hundreds of milliseconds of post-bounce accretion as a result of a temperature inversion near the neutrinosphere.

2. The mass of the proto-neutron star emerges as the single most important parameter regulating the secular rise of the mean neutrino energies, at least for a given equation of state. For individual models, we find that the electron antineutrino mean energy  $\langle E_{\bar{\nu}_e} \rangle$  scales very well with the proto-neutron star mass  $M$ ,

$$\langle E_{\bar{\nu}_e} \rangle \propto M. \quad (34)$$

The proportionality constant is slightly progenitor-dependent. This scaling is a consequence of the roughly adiabatic stratification of the hot accretion mantle of the proto-neutron star between nuclear density and the neutrinosphere and the steepness of the mass-radius relation between  $0.5M_\odot$  and  $2M_\odot$  for nucleonic equations of state (Lattimer & Prakash 2007; Steiner et al. 2010).

3. After shock revival, our 2D models differ considerably from artificial 1D explosion models (Fischer et al. 2010). We find that there is no abrupt drop of the electron neutrino and antineutrino luminosity to indicate the onset of the explosion because accretion downflows persist for a long time and transport fresh material to the cooling region. The accretion luminosity therefore remains high and can even rise transiently due to early fallback.
4. The neutrino signal from a Galactic supernova could provide *time-dependent* information about the dynamics in the supernova core at least for distances  $\leq 10$  kpc if the survival probability of electron antineutrinos is high. In a detector like IceCube, strong SASI activity will reveal itself by a strong, narrow-banded modulation of the detection rate with a period of  $T_{\text{SASI}}$  that is directly related to the average shock radius  $r_{\text{sh}}$  and the proto-neutron star radius  $r_{\text{PNS}}$ :

$$T_{\text{SASI}} \approx 19 \text{ ms} \left( \frac{r_{\text{sh}}}{100 \text{ km}} \right)^{3/2} \ln \left( \frac{r_{\text{sh}}}{r_{\text{PNS}}} \right). \quad (35)$$

The amplitude of the signal modulation will depend on the observer direction, as will the presence of an overtone at  $T_{\text{SASI}}/2$ . For sustained SASI activity, the observed ‘‘SASI chirp’’ signal will directly reveal the expansion or contraction of the shock. Based on model s25, one might speculate that failing supernovae with a sufficient delay time to black hole collapse will generally be accompanied by a such ‘‘SASI neutrino chirp’’.

5. A wavelet-based time-frequency analysis of the observed signal in IceCube could also help to pinpoint the onset of the explosion. We predict that the explosion will be accompanied by a shift of the typical modulation frequency of the signal below  $40 \dots 50$  Hz. Moreover, the early fallback of shocked material onto the proto-neutron star through new downflows in (initially) weak explosions will lead to a detectable burst-like *increase* in the electron antineutrino luminosity. In the wavelet spectrogram of the signal, such events

would manifest themselves as localized vertical stripes stretching over an extended frequency range.

The temporal variations in the neutrino signal are obviously an intriguing diagnostics for the dynamics in the supernova core, but their robustness could be a potential concern. Our results are based on axisymmetric models (instead of full 3D simulations), rely on the assumption of a normal neutrino mass hierarchy and disregard possible non-linear flavor conversion due to neutrino-neutrino refraction. In our opinion, it is mainly the uncertainties in the neutrino physics that make it difficult to decide about the detectability of spatio-temporal variations in the neutrino signal. In the worst case of an inverted mass hierarchy, MSW conversion in the stellar envelope could lead to a complete swap of  $\bar{\nu}_e$  and  $\bar{\nu}_\mu$  (Dighe & Smirnov 2000). As the contribution of the accretion luminosity is small for  $\nu_\mu$ ’s and  $\nu_\tau$ ’s, this would reduce the amplitude of the signal fluctuations by a factor of several (Tamborra et al. 2013). Even under such pessimistic conditions, periodic fluctuations would remain detectable out to a few kpc at least for models with strong SASI activity like s25. However, neither our most optimistic case nor this pessimistic scenario might be realized in nature. Neutrino-neutrino refraction effects could lead to flavor swap for at least for certain neutrino energies (see Duan & Kneller 2009; Duan et al. 2010 for a review) already close to the neutrinosphere, which would in turn affect the outcome of MSW flavor conversion in the envelope. The precise conditions for non-linear neutrino flavor conversion (e.g. the interplay of neutrino-neutrino refraction with the ordinary matter affect and the role of a non-axisymmetric neutrino distribution in phase space) are a matter of active debate (Sawyer 2009; Sarikas et al. 2012a,b; Saviano et al. 2012; Cherry et al. 2012; Mirizzi & Serpico 2012; Raffelt & Seixas 2013; Raffelt et al. 2013). Moreover, the simple picture of adiabatic MSW flavor conversion in the envelope might not hold in the presence of sufficiently strong turbulent density perturbations in convection shells (Kneller & Volpe 2010; Kneller & Mauney 2013; Lund & Kneller 2013). These complications preclude any precise estimate about the amplitude of temporal fluctuations in the observed neutrino signal. However, uncertainties in the neutrino physics are unlikely to render these fluctuations completely undetectable for nearby supernovae driven by vigorous hydrodynamic instabilities.

Our use of the ray-by-ray-plus method for the neutrino transport instead of a full multi-angle treatment might also be a concern, but by reprocessing our ray-by-ray-plus results as described in Section 4.1, we ensure that we do not grossly overestimate the amplitude of the fluctuating neutrino signal.

The restriction of our current models to 2D is probably less of a concern, especially for clearly SASI-dominated models like s25 and s27. As demonstrated by Hanke et al. (2013), the SASI can grow no less vigorously in 3D under appropriate conditions, and the concomitant emission anisotropies are of similar magnitude as in our 2D models (see Tamborra et al. 2013). The viewing-angle dependence of SASI-induced neutrino flux variations may of course be different in 3D, where the SASI can also develop a spiral mode, and where both the sloshing axis and the plane of the spiral mode can be time-dependent.

It is evident that the temporal variations of the observable neutrino signal could prove a powerful diagnostic in the case of Galactic supernova, revealing much more than the mere presence of the SASI and an ‘‘average SASI’’ frequency as

discussed in previous studies (Marek & Janka 2009; Ott et al. 2008; Lund et al. 2010; Brandt et al. 2011; Lund et al. 2012; Tamborra et al. 2013). Together with time-dependent measurements of the neutrino flux and mean energy, the temporal variations in the neutrino signal could potentially provide much more than such overall constraints on the core mass and compactness as discussed previously in the literature (Bruenn 1987; Burrows 1988; O’Connor & Ott 2013), especially if gravitational wave spectra were also available to determine the surface g-mode frequency  $f$  of the proto-neutron star (with  $f(t) \propto GM/(r_{\text{PNS}}^2 \langle E_{\bar{\nu}_e} \rangle) (1 - GM/r_{\text{PNS}} c^2)^2$  as shown in Müller et al. 2013). The approximate mass-temperature relation  $\langle E_{\bar{\nu}_e} \rangle \propto M$  and the relation for the SASI chirp might then allow a (tentative) reconstruction of the parameters  $M(t)$  (proto-neutron star mass),  $r_{\text{PNS}}(t)$  (proto-neutron star radius), and  $r_{\text{sh}}(t)$  (shock radius) of the accretion flow in the pre-explosion phase.

Given the manifold uncertainties in predicting precise neutrino signal templates (neutrino flavor conversion, opacities in dense matter, equation-of-state dependence), it is, of course, obvious that the “signal inversion problem” is bound to remain a serious challenge in neutrino astronomy that goes far beyond the scope of this paper. We believe, however, that the work presented here may provide some useful ideas for interpreting future observations of core-collapse supernovae in neutrinos.

This work was supported by the Deutsche Forschungsgemeinschaft through the Transregional Collaborative Research Center SFB/TR 7 “Gravitational Wave Astronomy” and the Cluster of Excellence EXC 153 “Origin and Structure of the Universe” (<http://www.universe-cluster.de>). The computations were performed on the IBM p690 and the IBM iDataPlex system *hydra* of the Computer Center Garching (RZG), on the Curie supercomputer of the Grand Équipement National de Calcul Intensif (GENCI) under PRACE grant RA0796, on the Cray XE6 and the NEC SX-8 at the HLRS in Stuttgart (within project SuperN), on the JUROPA systems at the John von Neumann Institute for Computing (NIC) in Jülich (through grant HMu092 and through a DECI-7 project grant), and on the Itasca Cluster of the Minnesota Supercomputing Institute.

## REFERENCES

- Abbasi, R. et al. 2011, *A&A*, 535, A109  
Abe, K. et al. 2011, *ArXiv e-prints*, 1109.3262  
Aleksiev, E. N., Aleksieva, L. N., Volchenko, V. I., & Krivosheina, I. V. 1987, *Soviet Journal of Experimental and Theoretical Physics Letters*, 45, 589  
Arcones, A., & Thielemann, F.-K. 2013, *Journal of Physics G Nuclear Physics*, 40, 013201  
Arnett, W. D., Bahcall, J. N., Kirshner, R. P., & Woosley, S. E. 1989, *ARA&A*, 27, 629  
Beringer, J. et al. 2012, *Phys. Rev. D*, 86, 010001  
Bethe, H. A. 1990, *Rev. Mod. Phys.*, 62, 801  
Bethe, H. A., & Wilson, J. R. 1985, *ApJ*, 295, 14  
Bionta, R. M., Blewett, G., Bratton, C. B., Casper, D., & Ciocio, A. 1987, *Physical Review Letters*, 58, 1494  
Blondin, J. M., & Mezzacappa, A. 2006, *ApJ*, 642, 401  
Blondin, J. M., Mezzacappa, A., & DeMarino, C. 2003, *ApJ*, 584, 971  
Brandt, T. D., Burrows, A., Ott, C. D., & Livne, E. 2011, *ApJ*, 728, 8  
Bruenn, S. W. 1985, *ApJS*, 58, 771  
—. 1987, *Physical Review Letters*, 59, 938  
Bruenn, S. W., Dirk, C. J., Mezzacappa, A., Hayes, J. C., Blondin, J. M., Hix, W. R., & Messer, O. E. B. 2006, *J. Phys. Conf. Ser.*, 46, 393  
Bruenn, S. W. et al. 2013, *ApJ*, 767, L6  
Buras, R., Janka, H.-T., Keil, M. T., Raffelt, G. G., & Rampp, M. 2003, *ApJ*, 587, 320  
Buras, R., Janka, H.-T., Rampp, M., & Kifonidis, K. 2006a, *A&A*, 457, 281  
Buras, R., Rampp, M., Janka, H.-T., & Kifonidis, K. 2006b, *A&A*, 447, 1049  
Burrows, A. 1988, *ApJ*, 334, 891  
—. 1990, *Annual Review of Nuclear and Particle Science*, 40, 181  
—. 2013, *Reviews of Modern Physics*, 85, 245  
Burrows, A., Hayes, J., & Fryxell, B. A. 1995, *ApJ*, 450, 830  
Burrows, A., & Sawyer, R. F. 1998, *Phys. Rev. C*, 58, 554  
Burrows, A., Young, T., Pinto, P., Eastman, R., & Thompson, T. A. 2000, *ApJ*, 539, 865  
Carter, G. W., & Prakash, M. 2002, *Physics Letters B*, 525, 249  
Chakraborty, S., Fischer, T., Mirizzi, A., Saviano, N., & Tomàs, R. 2011, *Physical Review Letters*, 107, 151101, 1104.4031  
Cherry, J. F., Carlson, J., Friedland, A., Fuller, G. M., & Vlasenko, A. 2012, *Physical Review Letters*, 108, 261104  
Colella, P., & Woodward, P. R. 1984, *J. Comp. Phys.*, 54, 174  
Cordero-Carrión, I., Cerdá-Durán, P., Dimmelmeyer, H., Jaramillo, J. L., Novak, J., & Gourgoulhon, E. 2009, *Phys. Rev. D*, 79, 024017  
Demorest, P. B., Pennucci, T., Ransom, S. M., Roberts, M. S. E., & Hessels, J. W. T. 2010, *Nature*, 467, 1081  
Dighe, A. S., & Smirnov, A. Y. 2000, *Phys. Rev. D*, 62, 033007  
Duan, H., Fuller, G. M., & Qian, Y.-Z. 2010, *Annual Review of Nuclear and Particle Science*, 60, 569  
Duan, H., & Kneller, J. P. 2009, *Journal of Physics G Nuclear Physics*, 36, 113201  
Fernández, R. 2010, *ApJ*, 725, 1563  
Fernández, R., & Thompson, C. 2009, *ApJ*, 703, 1464  
Fischer, T., Martínez-Pinedo, G., Hempel, M., & Liebendörfer, M. 2012, *Phys. Rev. D*, 85, 083003  
Fischer, T., Whitehouse, S. C., Mezzacappa, A., Thielemann, F., & Liebendörfer, M. 2010, *A&A*, 517, A80+  
Fischer, T., Whitehouse, S. C., Mezzacappa, A., Thielemann, F.-K., & Liebendörfer, M. 2009, *A&A*, 499, 1  
Foglizzo, T., Galletti, P., Scheck, L., & Janka, H.-T. 2007, *ApJ*, 654, 1006  
Foglizzo, T., Scheck, L., & Janka, H.-T. 2006, *ApJ*, 652, 1436  
Halzen, F., & Raffelt, G. G. 2009, *Phys. Rev. D*, 80, 087301  
Hanke, F., Müller, B., Wongwathanarat, A., Marek, A., & Janka, H.-T. 2013, *ApJ*, 770, 66  
Hannestad, S., & Raffelt, G. 1998, *ApJ*, 507, 339  
Herant, M., Benz, W., & Colgate, S. 1992, *ApJ*, 395, 642  
Herant, M., Benz, W., Hix, W. R., Fryer, C. L., & Colgate, S. A. 1994, *ApJ*, 435, 339  
Hirata, K., Kajita, T., Koshiba, M., Nakahata, M., & Oyama, Y. 1987, *Physical Review Letters*, 58, 1490  
Horowitz, C. J. 1997, *Phys. Rev. D*, 55, 4577  
—. 2002, *Phys. Rev. D*, 65, 043001  
Hüdepohl, L., Müller, B., Janka, H., Marek, A., & Raffelt, G. G. 2009, *Phys. Rev. Lett.*  
Iwakami, W., Kotake, K., Ohnishi, N., Yamada, S., & Sawada, K. 2008, *ApJ*, 678, 1207  
—. 2009, *ApJ*, 700, 232  
Janka, H.-T. 2012, *Annual Review of Nuclear and Particle Science*, 62, 407  
Janka, H.-T., Hanke, F., Hüdepohl, L., Marek, A., Müller, B., & Obergaulinger, M. 2012, *Progress of Theoretical and Experimental Physics*, 2012, 010000  
Janka, H.-T., & Hillebrandt, W. 1989a, *A&AS*, 78, 375  
—. 1989b, *A&A*, 224, 49  
Janka, H.-T., & Müller, E. 1996, *A&A*, 306, 167  
Kachelrieß, M., Tomàs, R., Buras, R., Janka, H.-T., Marek, A., & Rampp, M. 2005, *Phys. Rev. D*, 71, 063003  
Keil, M. T., Raffelt, G. G., & Janka, H.-T. 2003, *ApJ*, 590, 971  
Keil, W., Janka, H.-T., Schramm, D. N., Sigl, G., Turner, M. S., & Ellis, J. 1997, *Phys. Rev. D*, 56, 2419  
Kneller, J., & Volpe, C. 2010, *Phys. Rev. D*, 82, 123004  
Kneller, J. P., & Mauney, A. W. 2013, *Phys. Rev. D*, 88, 025004  
Koshiba, M. 1992, *Phys. Rep.*, 220, 229  
Kotake, K., Sumiyoshi, K., Yamada, S., Takiwaki, T., Kuroda, T., Suwa, Y., & Nagakura, H. 2012a, *Progress of Theoretical and Experimental Physics*, 2012, 301  
Kotake, K., Takiwaki, T., Suwa, Y., Iwakami Nakano, W., Kawagoe, S., Masada, Y., & Fujimoto, S.-i. 2012b, *Advances in Astronomy*, 2012  
Langanke, K. et al. 2003, *Physical Review Letters*, 90, 241102  
Langanke, K., Martínez-Pinedo, G., Müller, B., Janka, H.-T., Marek, A., Hix, W. R., Juodagalvis, A., & Sampaio, J. M. 2008, *Phys. Rev. Lett.*, 100, 011101:1  
Lattimer, J. M., & Prakash, M. 2007, *Phys. Rep.*, 442, 109  
Lattimer, J. M., & Swesty, F. D. 1991, *Nucl. Phys. A*, 535, 331  
Lentz, E. J., Mezzacappa, A., Bronson Messer, O. E., Hix, W. R., & Bruenn, S. W. 2012a, *ApJ*, 760, 94  
Lentz, E. J., Mezzacappa, A., Bronson Messer, O. E., Liebendörfer, M., Hix, W. R., & Bruenn, S. W. 2012b, *ApJ*, 747, 73  
Liebendörfer, M., Messer, O. E. B., Mezzacappa, A., Bruenn, S. W., Cardall, C. Y., & Thielemann, F.-K. 2004, *ApJS*, 150, 263  
Liebendörfer, M., Mezzacappa, A., Messer, O. E. B., Martínez-Pinedo, G., Hix, W. R., & Thielemann, F.-K. 2003, *Nuclear Physics A*, 719, 144  
Lund, T., & Kneller, J. P. 2013, *Phys. Rev. D*, 88, 023008  
Lund, T., Marek, A., Lunardini, C., Janka, H., & Raffelt, G. 2010, *Phys. Rev. D*, 82, 063007

- Lund, T., Wongwathanarat, A., Janka, H.-T., Müller, E., & Raffelt, G. 2012, *Phys. Rev. D*, 86, 105031
- Marek, A., & Janka, H. 2009, *ApJ*, 694, 664
- Marek, A., Janka, H., & Müller, E. 2009, *A&A*, 496, 475
- Martínez-Pinedo, G., Fischer, T., Lohs, A., & Huther, L. 2012, *Physical Review Letters*, 109, 251104
- Mayle, R., Wilson, J. R., & Schramm, D. N. 1987, *ApJ*, 318, 288
- Mezzacappa, A., & Bruenn, S. W. 1993, *ApJ*, 405, 669
- Mignone, A., & Bodo, G. 2005, *MNRAS*, 364, 126
- Mihalas, D., & Weibel Mihalas, B. 1984, *Foundations of radiation hydrodynamics* (New York: Oxford University Press)
- Mirizzi, A. 2013, *Phys. Rev. D*, 88, 073004
- Mirizzi, A., & Serpico, P. D. 2012, *Physical Review Letters*, 108, 231102
- Müller, B., Janka, H., & Dimmelmeier, H. 2010, *ApJS*, 189, 104
- Müller, B., Janka, H.-T., & Heger, A. 2012a, *ApJ*, 761, 72
- Müller, B., Janka, H.-T., & Marek, A. 2012b, *ApJ*, 756, 84
- . 2013, *ApJ*, 766, 43
- Müller, E., & Janka, H.-T. 1997, *A&A*, 317, 140
- Müller, E., Janka, H.-T., & Wongwathanarat, A. 2012c, *A&A*, 537, A63
- Nakazato, K., Sumiyoshi, K., Suzuki, H., Totani, T., Umeda, H., & Yamada, S. 2013, *ApJS*, 205, 2
- O'Connor, E., & Ott, C. D. 2013, *ApJ*, 762, 126
- Ohnishi, N., Kotake, K., & Yamada, S. 2006, *ApJ*, 641, 1018
- Ott, C. D., Burrows, A., Dessart, L., & Livne, E. 2008, *ApJ*, 685, 1069
- Peres, B., Penner, A. J., Novak, J., & Bonazzola, S. 2014, *Classical and Quantum Gravity*, 31, 045012
- Pons, J. A., Miralles, J. A., & Ibanez, J. M. A. 1998, *A&AS*, 129, 343
- Quirk, J. J. 1994, *Int. J. Num. Meth. in Fluids*, 18, 555
- Radice, D., Abdikamalov, E., Rezzolla, L., & Ott, C. D. 2013, *Journal of Computational Physics*, 242, 648
- Raffelt, G., Sarikas, S., & Seixas, D. d. S. 2013, *Physical Review Letters*, 111, 091101
- Raffelt, G., & Seixas, D. d. S. 2013, *Phys. Rev. D*, 88, 045031
- Raffelt, G. G. 2001, *ApJ*, 561, 890
- Rampp, M., & Janka, H.-T. 2002, *A&A*, 396, 361
- Reddy, S., Prakash, M., Lattimer, J. M., & Pons, J. A. 1999, *Phys. Rev. C*, 59, 2888
- Roberts, L. F. 2012, *ApJ*, 755, 126
- Roberts, L. F., Reddy, S., & Shen, G. 2012a, *Phys. Rev. C*, 86, 065803
- Roberts, L. F., Shen, G., Cirigliano, V., Pons, J. A., Reddy, S., & Woosley, S. E. 2012b, *Physical Review Letters*, 108, 061103
- Salathe, M., Ribordy, M., & Demirörs, L. 2012, *Astroparticle Physics*, 35, 485
- Sarikas, S., Raffelt, G. G., Hüdepohl, L., & Janka, H.-T. 2012a, *Physical Review Letters*, 108, 061101
- Sarikas, S., Tamborra, I., Raffelt, G., Hüdepohl, L., & Janka, H.-T. 2012b, *Phys. Rev. D*, 85, 113007
- Saviano, N., Chakraborty, S., Fischer, T., & Mirizzi, A. 2012, *Phys. Rev. D*, 85, 113002
- Sawyer, R. F. 2009, *Phys. Rev. D*, 79, 105003
- Scheck, L., Janka, H.-T., Foglizzo, T., & Kifonidis, K. 2008, *A&A*, 477, 931
- Scholberg, K. 2012, *Annual Review of Nuclear and Particle Science*, 62, 12072
- Serpico, P. D., Chakraborty, S., Fischer, T., Hüdepohl, L., Janka, H.-T., & Mirizzi, A. 2012, *Phys. Rev. D*, 85, 085031
- Shen, H., Toki, H., Oyamatsu, K., & Sumiyoshi, K. 1998, *Nucl. Phys. A*, 637, 435
- Steiner, A. W., Lattimer, J. M., & Brown, E. F. 2010, *ApJ*, 722, 33
- Sumiyoshi, K., Yamada, S., & Suzuki, H. 2008, *ApJ*, 688, 1176
- Sumiyoshi, K., Yamada, S., Suzuki, H., Shen, H., Chiba, S., & Toki, H. 2005, *ApJ*, 629, 922
- Suwa, Y., Takiwaki, T., Kotake, K., Fischer, T., Liebendörfer, M., & Sato, K. 2013, *ApJ*, 764, 99
- Tamborra, I., Hanke, F., Müller, B., Janka, H.-T., & Raffelt, G. 2013, *Physical Review Letters*, 111, 121104, 1307.7936
- Tamborra, I., Müller, B., Hüdepohl, L., Janka, H.-T., & Raffelt, G. 2012, *Phys. Rev. D*, 86, 125031
- Thompson, T. A., Burrows, A., & Pinto, P. A. 2003, *ApJ*, 592, 434
- Woosley, S. E., Heger, A., & Weaver, T. A. 2002, *Rev. Mod. Phys.*, 74, 1015
- Woosley, S. E., & Weaver, T. A. 1995, *ApJS*, 101, 181
- Wurm, M. et al. 2012, *Astroparticle Physics*, 35, 685
- Yamada, S. 1997, *ApJ*, 475, 720

## APPENDIX

### NOISE LEVEL FOR THE DISCRETE WAVELET TRANSFORM

In order to compute the expectation value  $\langle |\chi(t, p)|^2 \rangle$  of the absolute square of the wavelet transform due to the background, we consider the discrete version of Equation (27):

$$\chi(t_i, p_k) = \frac{1}{\sqrt{|p_k|}} \sum_{i=1}^N \mathfrak{B}(t_i) \psi^* \left( \frac{t_i - t_l}{p_k} \right) \Delta t. \quad (\text{A1})$$

Here,  $\mathfrak{B}(t_i)$  is a random variable denoting the number of background events in the  $i$ -th time bin.

We may assume without loss of generality that  $t_l = 0$  and compute a time-independent expectation value  $\langle |\chi(p_k)|^2 \rangle$  for the background.  $\langle |\chi(p_k)|^2 \rangle$  is given by

$$\langle |\chi(p_k)|^2 \rangle = \frac{1}{|p_k|} \sum_{i=1}^N \sum_{j=1}^N \langle \mathfrak{B}(t_i) \mathfrak{B}(t_j) \rangle \psi^* \left( \frac{t_i}{p_k} \right) \psi \left( \frac{t_j}{p_k} \right) \Delta t^2. \quad (\text{A2})$$

For uncorrelated Poissonian noise in all the different time bins, we have

$$\langle \mathfrak{B}(t_i) \mathfrak{B}(t_j) \rangle = \begin{cases} \langle \mathfrak{B}(t_i) \rangle \langle \mathfrak{B}(t_j) \rangle = \langle \mathfrak{B} \rangle^2, & i \neq j, \\ \langle \mathfrak{B}(t_i)^2 \rangle = 2\langle \mathfrak{B} \rangle^2, & i = j. \end{cases} \quad (\text{A3})$$

Here,  $\langle \mathfrak{B} \rangle = \mathfrak{R}_0$  is the (time-independent) expectation value of  $\mathfrak{B}(t_i)$ . This implies that  $\langle |\chi(p_k)|^2 \rangle$  is given by

$$\begin{aligned} \langle |\chi(p_k)|^2 \rangle &= \frac{\Delta t^2}{|p_k|} \sum_{i=1}^N \sum_{j=1}^N \mathfrak{R}_0^2 (1 + \delta_{ij}) \psi^* \left( \frac{t_i}{p_k} \right) \psi \left( \frac{t_j}{p_k} \right) \\ &= \frac{\Delta t^2}{|p_k|} \left[ \sum_{i=1}^N \mathfrak{R}_0^2 \left| \psi \left( \frac{t_i}{p_k} \right) \right|^2 + \sum_{i=1}^N \sum_{j=1}^N \mathfrak{R}_0^2 \psi^* \left( \frac{t_i}{p_k} \right) \psi \left( \frac{t_j}{p_k} \right) \right] \\ &= \frac{\Delta t^2}{|p_k|} \left[ \sum_{i=1}^N \mathfrak{R}_0^2 \left| \psi \left( \frac{t_i}{p_k} \right) \right|^2 + \mathfrak{R}_0^2 \left| \sum_{i=1}^N \psi \left( \frac{t_i}{p_k} \right) \right|^2 \right] \\ &= \frac{\mathfrak{R}_0^2 \Delta t^2}{|p_k|} \left[ \sum_{i=1}^N \left| \psi \left( \frac{t_i}{p_k} \right) \right|^2 + \left| \sum_{i=1}^N \psi \left( \frac{t_i}{p_k} \right) \right|^2 \right]. \end{aligned} \quad (\text{A4})$$